Atmospheric Latent Heating Distributions in the Tropics Derived from Satellite Passive Microwave Radiometer Measurements

WILLIAM S. OLSON

JCET/University of Maryland, Baltimore County, Baltimore, Maryland

CHRISTIAN D. KUMMEROW

Mesoscale Atmospheric Processes Branch, NASA/Goddard Space Flight Center, Greenbelt, Maryland

YE HONG

Caelum Research Corporation, Rockville, Maryland

WEI-KUO TAO

Mesoscale Atmospheric Processes Branch, NASA/Goddard Space Flight Center, Greenbelt, Maryland

(Manuscript received 2 December 1997, in final form 30 August 1998)

ABSTRACT

A method for the remote sensing of three-dimensional latent heating distributions in precipitating tropical weather systems from satellite passive microwave observations is presented. In this method, cloud model simulated hydrometeor/latent heating vertical profiles that have radiative characteristics consistent with a given set of multispectral microwave radiometric observations are composited to create a best estimate of the observed profile. An estimate of the areal coverage of convective precipitation within the radiometer footprint is used as an additional constraint on the contributing model profiles. This constraint leads to more definitive retrieved profiles of precipitation and latent heating in synthetic data tests.

The remote sensing method is applied to Special Sensor Microwave/Imager (SSM/I) observations of tropical systems that occurred during the TOGA COARE Intensive Observing Period, and to observations of Hurricane Andrew (1992). Although instantaneous estimates of rain rates are high-biased with respect to coincident radar rain estimates, precipitation patterns are reasonably correlated with radar patterns, and composite rain rate and latent heating profiles show respectable agreement with estimates from forecast models and heat and moisture budget calculations. Uncertainties in the remote sensing estimates of precipitation/latent heating may be partly attributed to the relatively low spatial resolution of the SSM/I and a lack of microwave sensitivity to tenuous anvil cloud, for which upper-tropospheric latent heating rates may be significant. Estimated latent heating distributions in Hurricane Andrew exhibit an upper-level heating maximum that strengthens as the storm undergoes a period of intensification.

1. Introduction

The spatial and temporal distributions of atmospheric heating in the Tropics may have an important impact on large-scale circulations and climatic variability (Simpson et al. 1988). Using a steady-state, linearized primitive equation model Hartmann et al. (1984) demonstrated that the strength and vertical structure of the Walker circulation depend on the vertical distributions of diabatic heating in the atmosphere. In particular, a heating distribution with a maximum at ~400 mb, which is characteristic of mature cloud clusters, produced a circulation centered at the observed altitude with the proper westward tilt, whereas a ''convective'' heating profile with a midlevel heating maximum did not. DeMaria (1985) obtained best agreement between simulated and observed large-scale circulations over South America using a stationary heating profile with an upper-level (above 400 mb) maximum.

The possible role of diabatic heating in the generation of 30–60-day oscillations in the tropical atmosphere has been studied in several investigations. Lau and Peng (1987) simulated eastward-propagating Kelvin wave modes that are sustained through a ''mobile'' wave-CISK (conditional instability of the second kind) mech-

Corresponding author address: Dr. William S. Olson, NASA/GSFC, Code 912, Greenbelt, MD 20771.
E-mail: olson@agnes.gsfc.nasa.gov

© 1999 American Meteorological Society

anism. In their study, although the magnitude of the total columnar heating was parameterized in terms of surface convergence and saturation humidity, the vertical profile *shape* was prescribed, with a maximum near 400 mb. The simulated Kelvin wave circled the globe at the equator with a speed of $\sim$19 m s^{-1}, resulting in an oscillation period of only 24 days. The linear analysis of Chang and Lim (1988) demonstrated that the nature of equatorial Kelvin CISK modes is sensitive to the vertical distribution of heating: heating with a maximum in the lower troposphere resulted in a stationary unstable mode, while a heating profile with a maximum in the midtroposphere led to an eastward-propagating CISK mode with a phase speed between 15 and 30 m s^{-1}. Subsequently Sui and Lau (1989) examined the impact of different vertical heating profiles, sea surface temperatures, and boundary layer heating on the amplitude and speed of equatorial wave-CISK modes. Model simulations that included a deep heating profile, with maximum heating near 300 mb, resulted in a ''fast'' mode that circled the globe in 26 days, while a profile with a lower-level heating maximum between 500 and 700 mb produced a ''slow'' mode with a period of 52 days.

In the aforementioned studies, simplified models of the atmosphere were utilized to examine the possible relationships between diabatic heating and the dynamics of the tropical atmosphere. Ultimately, simulations from global general circulation models (GCMs), which include detailed descriptions of the physical processes in the atmosphere as well as the interactions with the underlying ocean–land surfaces, will be needed to better quantify these relationships. Independent measurements of atmospheric diabatic heating distributions would be useful not only for validating GCM simulations, but also to serve as additional input data to constrain global model simulations (see Krishnamurti et al. 1991; Kasahara et al. 1992). Knowledge of the space–time evolution of diabatic heating distributions in individual storms, such as tropical cyclones, is also useful for storm diagnostics and forecasting applications (Raymond et al. 1995; Peng and Chang 1996; Karyampudi et al. 1998).

Although estimates of diabatic heating may be deduced from analyses of rawinsonde network data (e.g., Yanai et al. 1973; Ogura and Cho 1973; Johnson 1976), the spatial coverage of these networks is extremely limited, especially if one considers the vast tropical oceanic regions that are nearly data void. Diabatic heating in individual storms may be inferred from Doppler radar divergence measurements (Mapes and Houze 1995), but this technique is limited to coverage by instrumented aircraft or ground stations.

In the present study, a physical method for retrieving latent heating distributions based upon satellite passive microwave radiometer measurements is developed to overcome the limitations of the ground- or aircraft-based methods. Currently the Special Sensor Microwave/Imager (SSM/I) instrument is operating on two Defense Military Satellite Program (DMSP) polar-orbiting satellites. The SSM/I is a passive microwave radiometer with dual-polarized channels at 19.35, 37, and 85.5 GHz, and a vertically polarized channel at 22.235 GHz. The Tropical Rainfall Measuring Mission (TRMM) observatory includes the TRMM Microwave Imager (TMI), a passive radiometer similar to SSM/I but having additional dual-polarized channels at 10.7 GHz and improved spatial resolution; see Kummerow et al. (1998). In addition, the Earth Observing System PM platform will include the Advanced Microwave Scanning Radiometer (AMSR), with dual-polarized channels at 6.925, 10.65, 18.7, 23.8, 36.5, and 89.0 GHz, and resolution comparable to the TMI; see Ashcroft and Wentz (1996). Measurements of upwelling microwave brightness temperatures provided by these radiometers are sensitive to the observed distributions of precipitating liquid and ice-phase hydrometeors. Since the mid-1970s, satellite microwave measurements have been utilized to estimate precipitation and hydrometeor water contents by many investigators. Since precipitation is the end-product of hydrometeor phase-change processes in clouds, and since latent heat is released/consumed by these processes, passive microwave measurements yield an indirect measurement of latent heating processes.

The relationship between hydrometeor distributions and latent heating is defined using the thermodynamic equation. Following Yanai et al. (1973) and Tao et al. (1993a), the thermodynamic equation is horizontally averaged to yield

$$c_p\overline{\pi}\left[\frac{\partial\overline{\theta}}{\partial t} + \overline{\mathbf{V}}\cdot\nabla\overline{\theta} + \overline{w}\frac{\partial\overline{\theta}}{\partial z}\right] = Q_1, \tag{1}$$

where

$$\overline{\pi} = (\overline{p}/1000\ \text{mb})^{R/c_p}. \tag{2}$$

Here, θ is the potential temperature, $\mathbf{V}$ is the horizontal wind vector, w is the vertical velocity, p is the pressure, R is the dry gas constant, c_p is the specific heat of air at constant pressure, and the overbars indicate horizontal averages. Therefore, the left-hand side of (1) represents the large-scale response to heating from the ''apparent'' heat source Q_1. The apparent heat source may be written

$$Q_1 = -c_p\overline{\pi}\frac{1}{\overline{\rho}}\frac{\partial\overline{\rho}\,\overline{w'\theta'}}{\partial z} + L_v(\overline{c} - \overline{e}) + L_f(\overline{f} - \overline{m}) + L_s(\overline{d} - \overline{s}) + \overline{Q}_R, \tag{3}$$

where ρ is the air density, and L_v, L_f, and L_s are the latent heats of vaporization, fusion, and sublimation, respectively. The variables c, e, f, m, d, and s are the rates of condensation, evaporation, freezing, melting, deposition, and sublimation per unit mass of air, respectively; Q_R is the radiative heating rate per unit mass of air; and primes indicate deviations from the horizontal averages. From (3) it is noted that contributions to the apparent heat source, Q_1, are from eddy flux convergence of heat (first term), latent heating (second, third, and fourth terms), and radiation (last term).

Moisture conservation leads to a relationship between the vertically integrating latent heating terms of (3) and the surface precipitation rate, R (Yanai et al. 1973):

$$\int_0^{z_{\text{top}}} \overline{\rho}[L_v(\overline{c} - \overline{e}) + L_s(\overline{d} - \overline{s}) + L_f(\overline{f} - \overline{m})]\, dz \approx \rho_l L_v R. \quad (4)$$

Here, ρ_l is the material density of liquid water (1 g cm^{-3}). The relation (4) is approximate since condensate may not immediately precipitate from clouds; however, a study of modeled squall lines by Tao et al. (1993a) indicated differences less than 10% between storm-total vertically integrated condensate and precipitation depth. It was also demonstrated by Tao et al. (1993a) that latent heating dominates the eddy flux convergence and radiation contributions to the total Q_1. It follows that passive microwave estimates of surface rainfall rate can yield reasonable estimates of vertically integrated latent heating, at least in the space–time average sense, and that these estimates will be close to the vertically integrated Q_1.

The relationship between the *vertical profile* of heating and hydrometeor distributions is more tenuous. This is because the heating rate is a function of not only the hydrometeor vertical distributions, but also the dynamics of the cloud environment. Tao et al. (1990) and Tao et al. (1993b) and Smith et al. (1994) have applied water substance conservation principles to vertical profiles of hydrometeors, given theoretical fallout rates for each hydrometeor species and an assumed vertical velocity profile. These authors assert that if the vertical profile of hydrometeors can be estimated from passive microwave measurements, then the associated latent heating rates can be obtained by imposing water substance conservation to each cloud layer under steady-state conditions. For example, a net flux convergence of liquid hydrometeors in a given cloud layer is balanced by removal of hydrometeors through microphysical processes such as evaporation or freezing, while a net flux divergence is balanced by processes such as condensation or melting.

A drawback of the conservation methods is that they are sensitive to the rates of change of hydrometeor water contents with height, and current passive microwave radiometers provide only limited information on vertical hydrometeor structure. Notwithstanding, Yang and Smith (1998) applied conservation principles with some success to SSM/I-retrieved hydrometeor profiles to obtain latent heating distributions in the Pacific warm-pool region. By subtracting their retrieved latent heating estimates from rawinsonde-derived estimates of the large-scale apparent moisture sink (Q_2; Yanai et al. 1973), these authors obtained mean eddy moisture flux convergence profiles that were consistent with average surface latent heat flux observations.

The potential difficulties of estimating hydrometeor profiles from remote sensing measurements prompted Tao et al. (1993b) to propose an alternative heating algorithm. Their ''convective–stratiform'' algorithm utilizes only the surface rain rate and an estimate of the fractions of rainfall produced by convective and stratiform processes. Model-generated convective and stratiform heating profiles, selected from a lookup table, are normalized by the convective and stratiform rainfall amounts assuming a relation such as (4) applies to both convective and stratiform rainfall regimes. The success of the method depends on the proper discrimination of convective and stratiform rain regimes, which have characteristic vertical motion and heating profile shapes: convective regions are associated with relatively strong lifting and heating through the depth of the troposphere, while stratiform regions are associated with weak lifting and heating aloft and subsidence and evaporative cooling at lower levels. The strong link between vertical velocity and diabatic heating rate is discussed by Anthes (1982) and Mapes and Houze (1995). W.-K. Tao et al. (1999, unpublished manuscript) applied the convective–stratiform algorithm to SSM/I-retrieved convective and stratiform rain amounts from the Tropical Ocean Global Atmosphere Coupled Ocean–Atmosphere Response Experiment (TOGA COARE) period to obtain vertical heating profiles. Agreement of his estimates with rawinsonde-derived Q_1 profiles depended upon an appropriate choice of model-simulated convective and stratiform heating profiles.

In the current study, a physically based algorithm is applied to passive microwave observations from the SSM/I to obtain estimates of surface rain rates, convective rain fractions, and latent heating profiles in tropical convective systems. It will be demonstrated that in addition to the seven SSM/I brightness temperature measurements at a given footprint location, measurements from neighboring footprints provide critical information regarding the convective–stratiform characteristics of the observed precipitation, and with this information more definitive estimates of the retrieved parameters are obtained. In section 2, cloud–radiative model simulations that support the retrieval algorithm are presented. The retrieval method is described in section 3, and tests of the method based upon model-generated ''synthetic'' brightness temperature data are presented in section 4. Applications of the retrieval method to SSM/I observations of the TOGA COARE study area and Hurricane Andrew are covered in section 5, and section 6 provides a summary and conclusions.

2. Cloud/radiative model simulations

a. Cloud-resolving model simulations

Cloud/radiative model simulations are based upon three-dimensional, nonhydrostatic, cloud-resolving numerical model simulations from the Goddard Cumulus Ensemble (GCE) model (Tao and Simpson 1993) and

the University of Wisconsin Nonhydrostatic Modeling System (UW-NMS; Tripoli, 1992a). The GCE model was initialized using National Oceanic and Atmospheric Administration (NOAA) P-3 flight-level data and rawinsonde observations of the environment in immediate advance of a tropical squall line, which occurred 22 February 1993, during TOGA COARE. A 1-km grid resolution GCE squall line simulation (TOGA1) on a 128 km × 128 km domain is described in Olson et al. (1996). A subsequent 3-km resolution squall line simulation on a 384 km × 384 km domain (TOGA3) exhibited storm structure similar to TOGA1, but initiation by a more extensive cool pool resulted in a much larger storm in the TOGA3 simulation. The extensive cool pool utilized in TOGA3 appears to be more consistent with aircraft observations; see Jorgensen et al. (1994).

Two additional simulations were performed using the UW-NMS. A tropical cyclone simulation (HURRICANE) was initiated using atmospheric observations made at Kingston, Jamaica, 36 h prior to the passage of Hurricane Gilbert (1988). Details of this simulation may be found in Tripoli (1992b). The final 6 h of the HURRICANE simulation utilized a 3.3-km resolution, 205 km × 205 km inner nest, from which atmospheric parameters were extracted for the current analysis. A second UW-NMS simulation of a thunderstorm complex observed during Cooperative Huntsville Meteorological Experiment (COHMEX) was performed on a 1-km resolution, 50 km × 50 km grid. Both the HURRICANE and COHMEX simulations are described in Panegrossi et al. (1998).

The simulated 3D model fields include pressure, temperature, relative humidity, and the hydrometeor water contents of nonprecipitating liquid cloud, rain, nonprecipitating ice cloud, snow, and graupel. Surface rainfall rates, R_{ij}, at each model grid element ij are determined from the simulations in a manner consistent with model physics. Rainfall rates in the GCE model runs are computed from the lowest model level raindrop size distributions. The fall velocity formula of Rutledge and Hobbs (1983) is applied to the simulated drop distribution at each model grid point to obtain the surface rainfall rate. Similarly, the fallout calculation described in Flatau et al. (1989) is applied to the raindrop size distributions at the lowest level of the UW-NMS simulations to obtain surface rain rates. In anticipation of retrieval algorithm applications to SSM/I data (section 3), grid-resolution rain rates from each model simulation are horizontally averaged over 12.5 km × 12.5 km areas to yield fields of the mean rain rate R. This resolution is consistent with the sampling resolution of the 85.5-GHz channels of the SSM/I.

Each horizontal grid point of the high-resolution model simulations is classified as convective or stratiform using the modified Churchill and Houze (1984) technique described in Tao et al. (1993a). The classified model fields are used to determine the convective area fractions and convective rain fractions over 12.5 km × 12.5 km areas from

$$f_A \equiv \frac{\sum_{i,j} A_{ij}\delta_{ij}}{\sum_{i,j} A_{ij}} \tag{5}$$

and

$$f_R \equiv \frac{\sum_{i,j} R_{ij}A_{ij}\delta_{ij}}{\sum_{i,j} R_{ij}A_{ij}}, \tag{6}$$

where

$$\delta_{ij} \equiv \begin{cases} 0, & \text{stratiform grid point;} \\ 1, & \text{convective grid point.} \end{cases} \tag{7}$$

Here, A_{ij} is the area of a model grid element, R_{ij} is the rain rate associated with that grid element, and the summations are over all grid elements within a given 12.5 km × 12.5 km area. Using (5), (6), and (7), f_A and f_R are calculated for each 12.5 km × 12.5 km area within the numerical model domains.

Latent heating profiles at grid resolution, $\mathrm{LH}(z)_{ij}$, are explicitly computed only in the TOGA3 GCE model simulation. In this case, the local latent heating rate per unit volume of air is given by

$$\mathrm{LH}(z)_{ij} = \rho_{ij}\{L_v(c_{ij} - e_{ij}) + L_s(d_{ij} - s_{ij}) + L_f(f_{ij} - m_{ij})\}. \tag{8}$$

In the TOGA1 GCE and HURRICANE and COHMEX UW-NMS simulations, latent heating profiles at model resolution are estimated from model-simulated thermodynamic and vertical velocity profiles using an approximate form of the first law of thermodynamics,

$$\mathrm{LH}(z)_{ij} \approx \rho_{ij}c_p w_{ij}\left(\frac{g}{c_p} + \left[\frac{dT}{dz}\right]_{ij}\right), \tag{9}$$

where g is the acceleration of gravity and dT/dz is the rate of change of temperature with height. Mapes and Houze (1995) used scaling arguments to demonstrate that the diabatic contribution to vertical motions dominates the adiabatic contribution in deep, long-lasting heated circulations. Also, since hydrometeor latent heating is a major contributor to the total diabatic heating in precipitating clouds as shown by Tao et al. (1993a), expression (9) is generally a reasonable approximation to the latent heating rate. Intercomparisons of explicitly calculated latent heating rates from the TOGA3 simulation and estimated latent heating rates from (9) are found to be in good agreement.

In anticipation of retrieval algorithm applications, the latent heating profiles at model grid resolution are horizontally averaged over 12.5 km × 12.5 km areas, and vertically averaged within 14 prescribed layers between the surface and 18-km altitude to produce mean profiles, $\mathrm{LH}(z)$. The latent heating profiles are layer averaged for

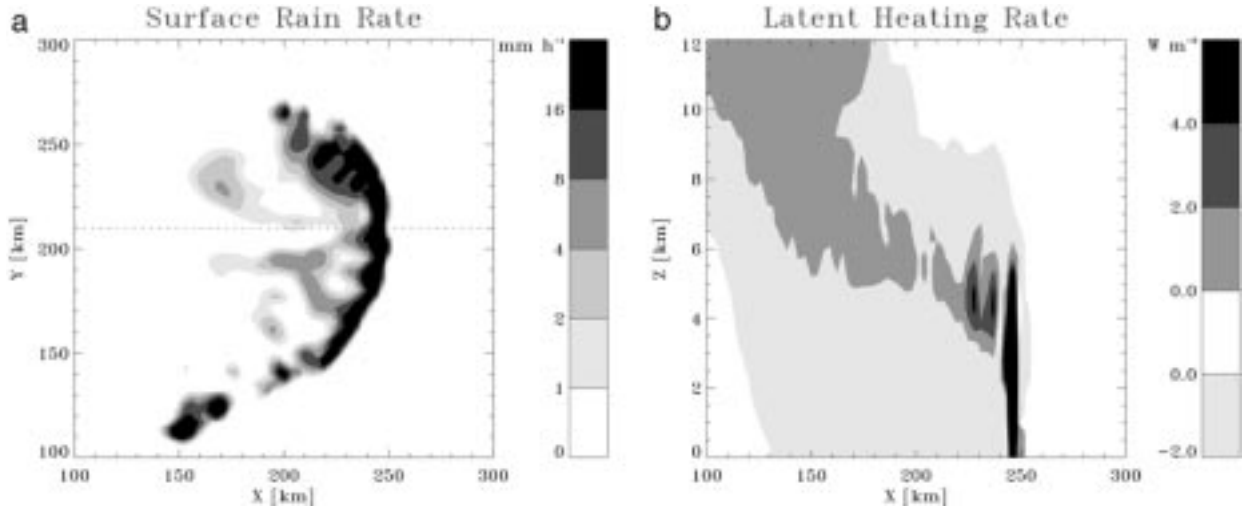

FIG. 1. Surface rainfall rate (a) and vertical cross section of latent heating rate at $Y = 210$ km (b) in a Goddard Cumulus Ensemble model simulation of the squall line observed 22 Feb 1993 during TOGA COARE. Both fields are generated at 300 min into the simulation.

the purpose of computational efficiency in retrieval applications. The contiguous layers are 0.5 km thick below 4-km altitude, 1.0 km thick from 4 to 6 km, 2.0 km thick between 6 and 10 km, and 4.0 km thick between 10 and 18 km.

b. Radiative transfer calculations

Microwave brightness temperatures at the SSM/I frequencies/polarizations are calculated from the high-resolution, model-simulated cloud fields using an Eddington radiative transfer routine. The resulting high-resolution (~1 km) fields of brightness temperatures are then convolved with the SSM/I antenna patterns to simulate antenna diffraction effects. A complete discussion of these brightness temperature calculations may be found in Kummerow et al. (1996). Finally, modeled atmospheric properties including R, f_A, f_R, and LH(z), which spatially coincide with the computed upwelling brightness temperatures, are filed with the brightness temperatures to produce a database suitable for diagnostic studies and retrieval applications; see section 3.

c. Precipitation and latent heating signatures

A plan view of surface rainfall rates from the TOGA3 simulation at 300 min is presented in Fig. 1a, and from the same simulation the vertical cross section of latent heating rates at $Y = 210$ km is displayed in Fig. 1b. Both fields are contoured, based upon the original, high-resolution GCE model output. The plan view of rain rates exhibits the structure of a mature tropical squall line, with a convex-shaped convective leading edge and a trailing region of stratiform precipitation. Rain rates along the convective leading edge typically exceed 16 mm h^{-1}, while in the stratiform region rain rates only occasionally exceed 4 mm h^{-1}. It may be noted from the cross section (Fig. 1b) that the convective leading edge is characterized by maximum latent heating rates exceeding 1.0 W m^{-3}, with positive latent heating confined to the lower and middle troposphere and only weak cooling above and in front of the convective line. Latent heating in the trailing stratiform region is much weaker, usually less than 0.5 W m^{-3}, with positive heating generally occurring above the freezing level (5.0 km) and evaporative cooling below the freezing level. These patterns of precipitation and latent heating are consistent with those reported by Tao et al. (1993b) in cloud modeling studies. Although latent heating rates cannot be measured directly, vertical motion fields in squall lines may be deduced from Doppler radar observations. If latent heating rate is nearly proportional to vertical velocity by (9), then the squall line vertical motion cross sections derived from Doppler radar by Hauser et al. (1988) and Biggerstaff and Houze (1993) imply latent heating distributions qualitatively similar to the model cross section in Fig. 1b. Braun and Houze (1996) derived convective and stratiform latent heating profiles from Doppler radar and rawinsonde observations of a midlatitude squall line. These heating profiles are also consistent with the model latent heating distribution shown in Fig. 1b.

Displayed in Figs. 2a and 2b are plan views of the vertically integrated precipitating liquid (rain) and ice (snow and graupel), respectively, from the TOGA3 simulation. Corresponding model-simulated, horizontally polarized brightness temperatures at the 19.35- and 85.5-GHz SSM/I frequencies are presented in Figs. 2c and 2d, respectively. The background is assumed to be a calm ocean surface. For the purpose of discussion, only the model grid-resolution brightness temperature fields are displayed (SSM/I antenna diffraction effects

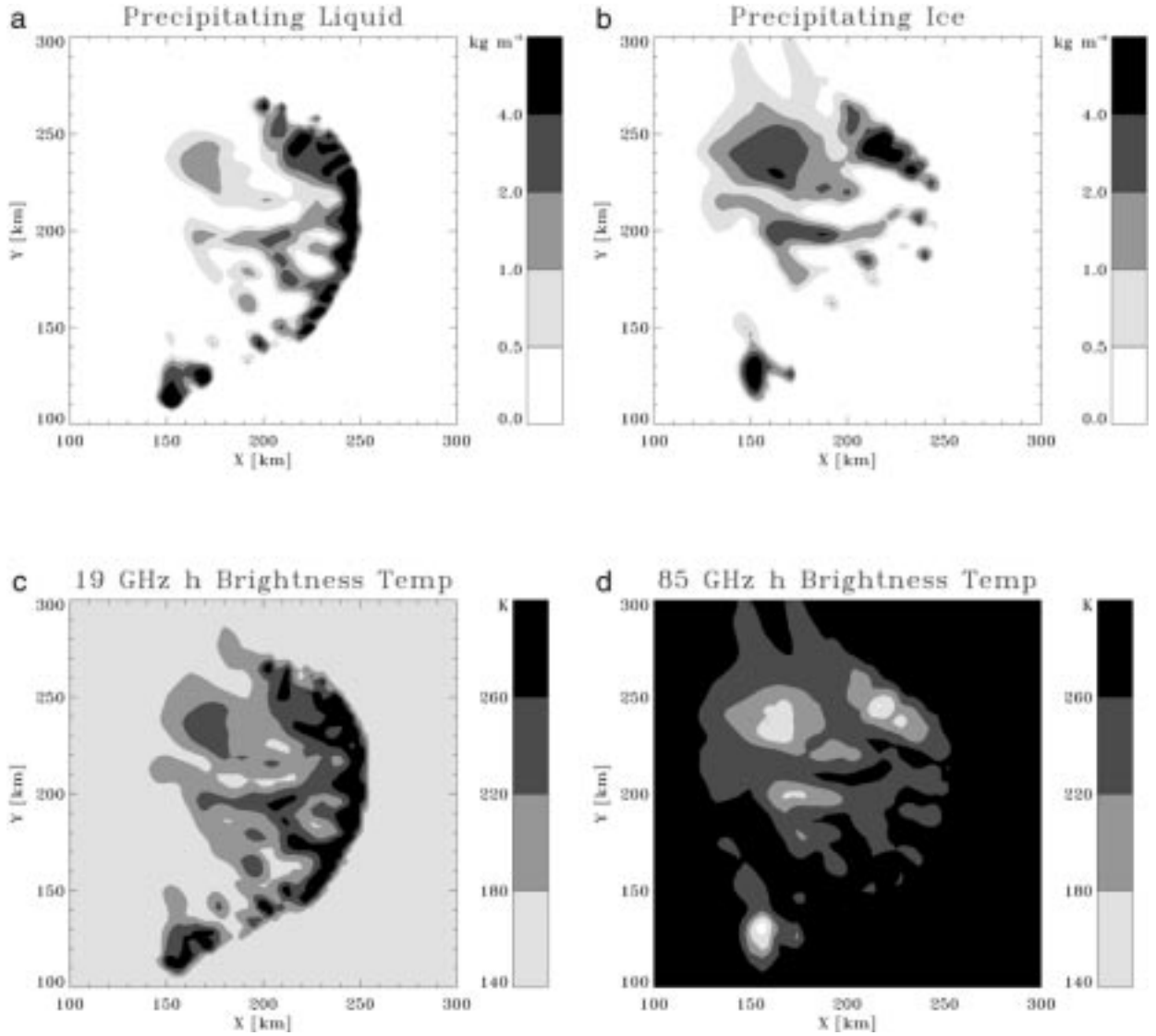

FIG. 2. Plan views of vertically integrated precipitating liquid (a), vertically integrated precipitating ice (b), upwelling brightness temperature at 19.35 GHz (c), and upwelling 85.5-GHz brightness temperature (d) derived from the Goddard Cumulus Ensemble model 300 min into a simulation of the squall line observed 22 Feb 1993 during TOGA COARE.

are omitted). Note that at 19.35 GHz, the brightness temperatures are correlated with the liquid precipitation pattern, since microwave emission from precipitating liquid water is the dominant contributor to the upwelling radiance. Brightness temperatures are generally the greatest along the convective leading edge, where liquid water contents are highest. In contrast, the upwelling brightness temperatures in precipitation-free regions are relatively low, due to the low emissivity of the ocean surface and the weak contribution from atmospheric absorption/emission. The 22.235- and 37-GHz brightness temperature fields (not shown) are similar to the field at 19.35 GHz, since emission from liquid precipitation usually dominates at these frequencies. The 85.5-GHz brightness temperatures are generally anticorrelated with precipitating ice contents. Microwave scattering by precipitation-sized ice particles tends to depress 85.5-GHz brightness temperatures with respect to ice-free regions. Ice-free regions are highly emissive due to a higher ocean emissivity and significant absorption/emission by atmospheric water vapor. These relationships between liquid and ice-phase hydrometeor water contents and upwelling brightness temperatures at the SSM/I frequencies are confirmed by several investigations, for example, Kummerow et al. (1996).

It may be inferred from the foregoing discussion that the 19.35- and 85.5-GHz SSM/I channels provide fairly independent information regarding liquid and ice-phase hydrometeor distributions over ocean backgrounds. In an attempt to further quantify the relationship between

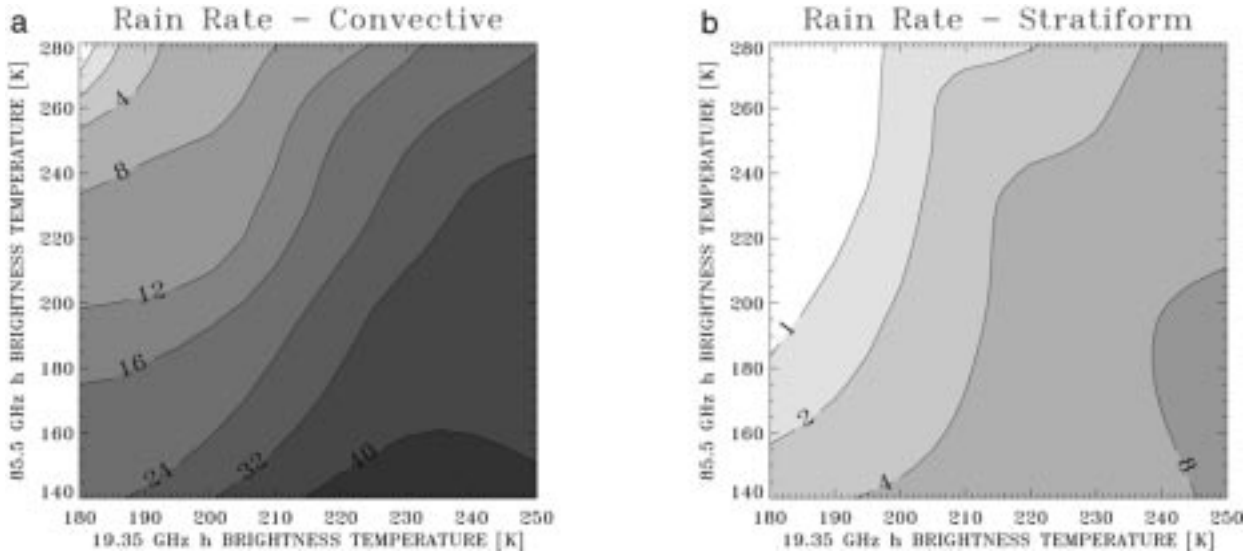

FIG. 3. Ensemble-mean, model-generated surface rainfall rates in mm h^{-1}, plotted as functions of simulated 19.35- and 85.5-GHz brightness temperatures from predominantly convective (a) and stratiform (b) regions.

surface rainfall rate and SSM/I brightness temperatures, the surface rain rates, R, at 12.5 km $\times$ 12.5 km resolution and horizontally polarized brightness temperatures at 19.35 and 85.5 GHz, including antenna diffraction effects, are analyzed as follows. First, each 12.5 km $\times$ 12.5 km model ''footprint'' is classified as convective or stratiform depending on the fraction of convective rain; if the convective rain fraction, f_R, is greater than 0.5, then the footprint is classified as convective, if f_R is less than 0.5, then the footprint is classified as stratiform. For each possible combination of 19.35- and 85.5-GHz brightness temperatures, the ensemble-mean rain rate over all simulated convective footprints is computed. The ensemble mean rain rates are plotted versus the 19.35- and 85.5-GHz brightness temperatures in Fig. 3a. The same procedure is applied to stratiform footprints, with the resulting plot shown in Fig. 3b. These plots represent the simple regression relationship between rain rates and the two selected brightness temperatures, and could be used to retrieve rain rate if only the 19.35- and 85.5-GHz horizontal SSM/I channels were available.

It may be noted from Fig. 3 that in general the surface rain rate increases with increasing 19.35-GHz brightness temperature (greater liquid water emission) and lower 85.5-GHz brightness temperature (greater ice scattering). However, for a given pair of brightness temperatures, the rain rate ''retrieved'' in a predominantly convective rain region is much higher than in a predominantly stratiform region. This difference is mainly due to the greater response of brightness temperatures to the average rainwater content if the rain field within the observed footprint is horizontally uniform, as is the case in stratiform regions (Kummerow 1998). It follows that if the convective–stratiform classification of the footprint is not known a priori, a large uncertainty in the surface rain rate estimate could result. Although the remaining SSM/I channels do provide additional information that can help reduce the uncertainty in rain estimates, the potential for ambiguity is clearly illustrated.

Plots similar to Fig. 3 are constructed for the model-simulated latent heating rates at the 3- and 7-km levels in Figs. 4a,b and Figs. 5a,b, respectively. Figures 4a,b depict the relationship between the latent heating rate at 3-km altitude and the 19.35- and 85.5-GHz brightness temperatures. The microwave signatures of low-level latent heating in convective and stratiform regions differ greatly. In convective regions, the low-level heating rate increases with increasing 19.35-GHz brightness temperature (and emission by liquid precipitation). However, the main trend in stratiform regions is greater cooling with decreasing 85.5-GHz brightness temperature. The greater overburden of ice-phase precipitation and increased microwave scattering at 85.5 GHz appear to be correlated with greater low-level evaporative cooling in stratiform regions. It has been suggested that the melting of anvil ice hydrometeors and subsequent evaporation of the rain produced both contribute to mesoscale descent and cooling at lower levels (Houze 1989).

The relationship between upper-level latent heating and brightness temperatures (Figs. 5a,b) is analogous to the relationship between rain rate and brightness temperatures seen in Fig. 3: latent heating rates increase with increasing 19.35-GHz brightness temperature and decreasing 85.5-GHz brightness temperature. Again, latent heating rates in convective regions are generally greater than those in stratiform regions for a given pair of brightness temperatures. This result is attributed to the greater horizontal inhomogeneity of the precipitation field in convective regions, which results in less micro-

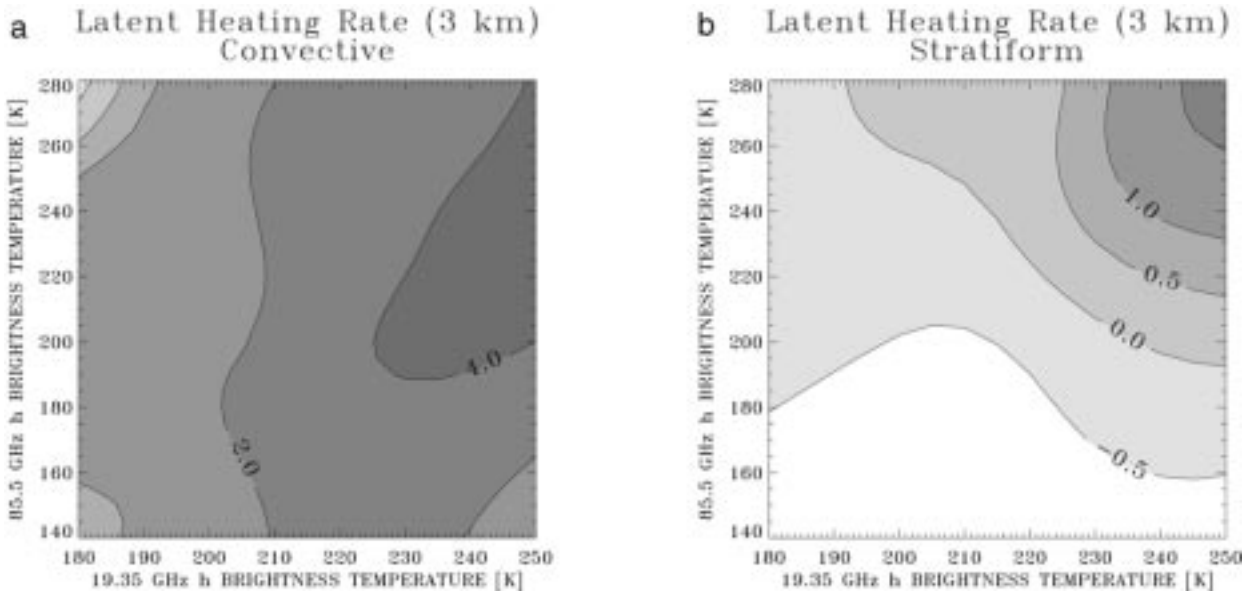

FIG. 4. Same as Fig. 3 but for model-generated latent heating rates in W m^{-3} at approximately 3-km altitude.

wave ''signal'' for a given liquid or ice-phase precipitation water content; see Kummerow (1998). The relationship between the rate of condensation/deposition and the ice precipitation water content may also differ in convective and stratiform regions, resulting in different ice scattering signatures for the same latent heating rate.

The foregoing analysis of simulated rain rates, latent heating rates, and microwave brightness temperatures indicates (a) significant sensitivity of SSM/I brightness temperatures to variations in rain rate and latent heating rates, and (b) different relationships between rain rate, latent heating rates, and SSM/I brightness temperatures depending on the proportion of convective–stratiform rain observed in a given footprint. Therefore, it may be possible to estimate rain rates and latent heating profiles from SSM/I observations, but unambiguous estimates will require either information from the remaining SSM/I channels (other than the 19.35- and 85.5-GHz horizontally polarized channels) or other contextual information to specify the convective–stratiform rain proportion.

3. Retrieval method

The basis of the retrieval method is the estimated expected value or ''Bayesian'' technique described in Kummerow et al. (1996) and Olson et al. (1996). In this method, the expected values of a set of retrieved parameters (the vector $\hat{\mathbf{E}}[\mathbf{x}]$) are estimated using

$$\hat{\mathbf{E}}[\mathbf{x}] = \sum_k \mathbf{x}_k \frac{\exp\{-0.5[\mathbf{TB}_O - \mathbf{TB}_S(\mathbf{x}_k)]^{\mathrm{T}}(\mathbf{O}_{\mathbf{TB}} + \mathbf{S}_{\mathbf{TB}})^{-1}[\mathbf{TB}_O - \mathbf{TB}_S(\mathbf{x}_k)]\}}{\hat{N}}. \tag{10}$$

Here, the vector $\mathbf{x}$ represents the set of all geophysical parameters considered in the retrieval, and the vectors $\mathbf{TB}_O$ and $\mathbf{TB}_S$ represent observed and computed sensor brightness temperatures, respectively; $\mathbf{O}_{\mathbf{TB}}$ and $\mathbf{S}_{\mathbf{TB}}$ are the error covariance matrices of the observed and computed brightness temperatures, respectively; and $\hat{N}$ is a normalization factor:

$$\hat{N} = \sum_k \exp\{-0.5[\mathbf{TB}_O - \mathbf{TB}_S(\mathbf{x}_k)]^{\mathrm{T}}(\mathbf{O}_{\mathbf{TB}} + \mathbf{S}_{\mathbf{TB}})^{-1} \times [\mathbf{TB}_O - \mathbf{TB}_S(\mathbf{x}_k)]\}. \tag{11}$$

In the present application, the right-hand side of (10) is a summation over the large ensemble of model-simulated atmospheric parameters $\mathbf{x}_k$ described in section 2. These parameters include the 12.5 km × 12.5 km area-average surface rainfall rate and latent heating rates in predefined layers. Corresponding to each 12.5 km × 12.5 km model footprint are the set of computed brightness temperatures, $\mathbf{TB}_S(\mathbf{x}_k)$, at the seven SSM/I frequencies/polarizations. As described in section 2, these computed brightness temperatures include simulated antenna diffraction effects, which degrade the horizontal

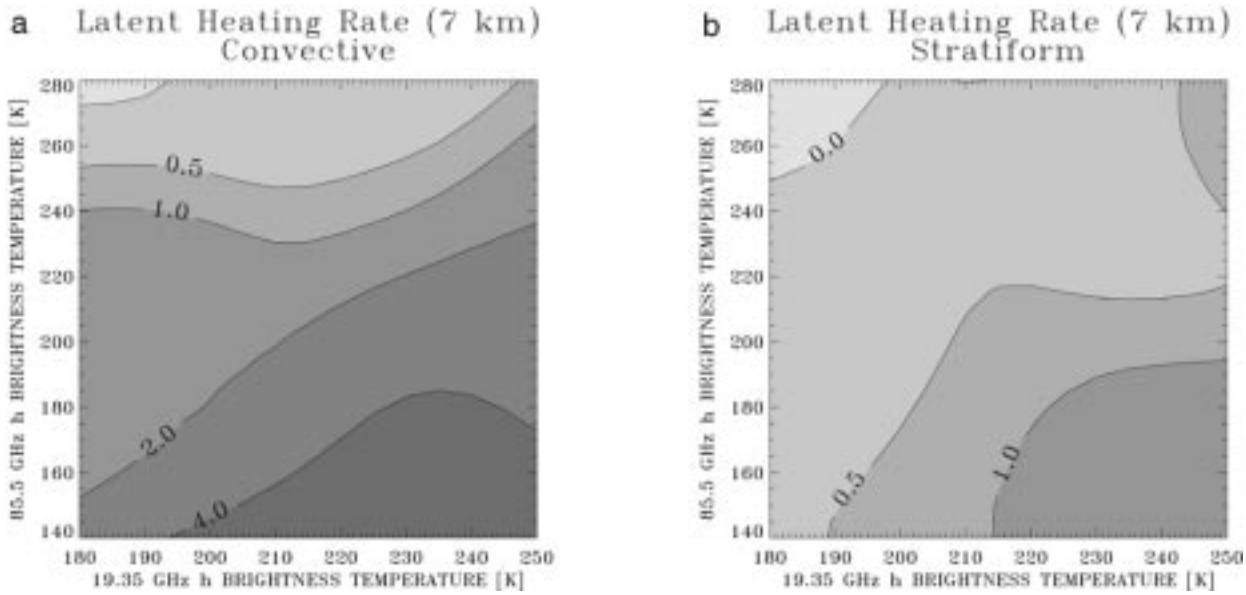

FIG. 5. Same as Fig. 3 but for model-generated latent heating rates in W m^{-3} at approximately 7-km altitude.

resolution of the SSM/I data. The vector $\mathbf{TB}_O$ represents a given set of seven SSM/I observed brightness temperatures. From (10) it is noted that the better the agreement between the computed brightness temperatures and observed brightness temperatures, the greater the weighting of parameters $\mathbf{x}_k$ in the summation. Therefore the estimate $\hat{\mathbf{E}}[\mathbf{x}]$ is a composite of the simulated parameters that are most radiatively consistent with the SSM/I observations.

In section 2 it was hypothesized that information regarding the proportion of convective–stratiform rain might be required to obtain unambiguous estimates of surface rain rate or latent heating rates. Anagnostou and Kummerow (1997) related the horizontal variability of 85.5-GHz scattering signatures from SSM/I to the percentage of stratiform rain in the field of view. Subsequently Hong et al. (1999) developed an index based upon the magnitudes of the scattering-induced depression and maximum horizontal gradient of SSM/I 85.5-GHz brightness temperatures. This index was found to be proportional to the areal fraction of convective rainfall within the SSM/I footprint. Also, the observational studies of Spencer et al. (1989) and Heymsfield and Fulton (1994a,b) and the radiative modeling of Petty and Turk (1996) and Schols et al. (1997) suggest that the difference between the 85.5-GHz vertically and horizontally polarized channels is relatively small (<5 K) in convective regions but larger in stratiform areas.

Motivated by these findings, an additional constraint is added to (10) to represent the difference between ''observed'' convective area fractions and model-simulated area fractions,

$$\hat{\mathbf{E}}[\mathbf{x}] = \sum_k \mathbf{x}_k \frac{\exp\{-0.5[\mathbf{TB}_O - \mathbf{TB}_S(\mathbf{x}_k)]^{\mathrm{T}}(\mathbf{O}_{\mathbf{TB}} + \mathbf{S}_{\mathbf{TB}})^{-1}[\mathbf{TB}_O - \mathbf{TB}_S(\mathbf{x}_k)] + C\}}{\hat{N}}, \tag{12}$$

where

$$\hat{N} = \sum_k \exp\{-0.5[\mathbf{TB}_O - \mathbf{TB}_S(\mathbf{x}_k)]^{\mathrm{T}}(\mathbf{O}_{\mathbf{TB}} + \mathbf{S}_{\mathbf{TB}})^{-1} \times [\mathbf{TB}_O - \mathbf{TB}_S(\mathbf{x}_k)] + C\} \tag{13}$$

and

$$C = -0.5[\mathbf{f}_{AO} - \mathbf{f}_{AS}(\mathbf{x}_k)]^{\mathrm{T}}(\mathbf{O}_f + \mathbf{S}_f)^{-1}[\mathbf{f}_{AO} - \mathbf{f}_{AS}(\mathbf{x}_k)]. \tag{14}$$

The vectors $\mathbf{f}_{AO}$ and $\mathbf{f}_{AS}$ represent the maximum observed and simulated convective area fractions, respectively, at different distances from a given satellite footprint (see Fig. 6). The first element of $\mathbf{f}_{AS}$ is given by (5) evaluated in region 1 of Fig. 6; the second element is the maximum convective area fraction in the 8 surrounding 12.5 km × 12.5 km boxes (region 2); the third element is the maximum convective area fraction in the 16 boxes surrounding the inner 9 boxes (region 3), and the fourth element is the maximum convective area fraction of the 24 boxes surrounding the inner 25 boxes (region 4). The

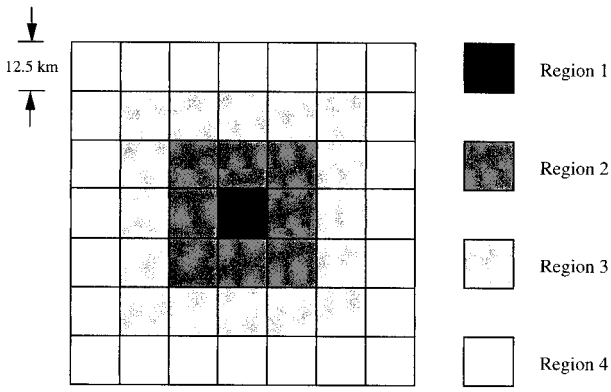

FIG. 6. Schematic of a 7 × 7 array of 85.5-GHz SSM/I observations. Shaded regions (1–4) are identified in the description of the convective area fraction constraint.

corresponding observed maximum convective area fractions, $\mathbf{f}_{AO}$, are determined from the passive microwave observations using empirical formulas; see section 5. Information from neighboring 12.5 km × 12.5 km grid boxes is utilized in the constraint (14) because studies such as Biggerstaff and Houze (1993) and Ferrier et al. (1996) have shown that the dynamical and microphysical properties of mesoscale convective systems vary as a function of distance from the convective updraft region. The error covariance matrices of the observed and simulated convective area fractions are $\mathbf{O}_f$ and $\mathbf{S}_f$, respectively.

4. Application of the retrieval method to synthetic observations

Due to the scarcity of reliable validation data and difficulties associated with the collocation of validation data and satellite measurements, a preliminary evaluation of the retrieval algorithm is performed using model-generated, synthetic observations. In the algorithm tests presented in this section, four of the 26 model-simulated atmospheres—TOGA1 at 180 min, TOGA3 at 240 min, HURRICANE at 3120 min, and COHMEX at 180 min—are set aside to serve as ''observed'' fields; the remaining 22 simulated atmospheres form the supporting database of the retrieval method; see section 3. Gaussian-distributed noise with a standard deviation of 1 K is added to the computed brightness temperatures associated with the observed fields to generate synthetic SSM/I observations. This noise level approximates SSM/I specifications (Hollinger et al. 1987). In each test, the algorithm (12) is applied to the synthetic SSM/I observations, and surface rainfall rates, convective rain flux fractions, and latent heating profiles are estimated. These estimated parameters are then compared to the known model-generated, ''true'' parameters, and error statistics are computed. Although similar tests of the retrieval method were performed by Kummerow et al. (1996), in these previous tests the retrieval of latent heating profiles was not attempted, and the retrieval method did not include a constraint on the convective area fraction as in (12). Also, in the present study the supporting database and synthetic observations have been expanded to include a more diverse set of model atmospheres.

First, a baseline application of the retrieval method to the synthetic data is performed in which the convective area fraction constraint C in (12) is set to zero. Next, the convective area fraction constraint is imposed using only the 12.5 km × 12.5 km box centered on the SSM/I observations (region 1 in Fig. 6). Finally, the full convective area fraction constraint is imposed using all grid boxes, including neighboring boxes in concentric ''rings'' surrounding the centered grid box (regions 1, 2, 3, and 4 in Fig. 6). Although different formulas have been proposed for estimating the convective area fraction based upon passive microwave observations (Hong et al. 1999), a generic definition of the convective fraction is employed here. Observations of $\mathbf{f}_{AO}$ are simulated by adding Gaussian-distributed noise with a standard deviation of 0.2 to the model-generated convective area fractions of the synthetic database. The added noise represents the potential uncertainty in remote sensing estimates of the convective area fraction. The same level of noise is added to the convective area fraction $\mathbf{f}_{AS}$ of the supporting database to represent errors in the cloud/radiative model simulations.

The influence of the constraint term relative to the brightness temperature term in (12) is dictated by the assumed uncertainty of the constraint. The diagonal elements $\mathbf{O}_f$ and $\mathbf{S}_f$ are the estimated error variances of the observed and simulated convective area fractions, respectively, while the off-diagonal elements are the error covariances. Consistent with the levels of noise added to the synthetic observed and simulated convective area fractions, σ_{Of} and σ_{Sf} are assigned a value of 0.2, while the off-diagonal elements of $\mathbf{O}_f$ and $\mathbf{S}_f$ are set to zero.

Listed in Tables 1 and 2 are the bias, error standard deviation, and correlation coefficient of the estimates of surface rain rate, convective rain flux fraction, vertically integrated latent heating rate, and mean heating rate in specified layers. Table 1 contains error statistics for algorithm applications over water surfaces, and Table 2 contains statistics for applications over land surfaces. Statistics of retrieved quantities from the baseline, centered grid box constraint, and full constraint algorithm applications are listed in the first, second, and third columns, respectively, under each statistic heading. At the resolution of the retrieval algorithm (12.5 km), estimates of surface rain rate and convective rain flux fraction over water surfaces benefit significantly from the imposed constraints, while the response of retrieved latent heating rates to the imposed constraints is mixed (Table 1). Moreover, estimated latent heating rates at lower elevations are rather weakly correlated with the true values. Similar trends are noted in the statistics of es-

TABLE 1. Statistics of synthetic retrievals over water surfaces. The three columns under each statistic correspond to estimates using no convective fraction constraint (first column), estimates using a convective fraction constraint on the central grid box only (second column), and estimates using a full convective fraction constraint (third column). Units of bias and error standard deviation are mm h^{-1} (rain rate), kW m^{-2} (vertically integrated latent heating rate), and W m^{-3} (layer-average latent heating rate).

Quantity	Bias			Error std dev			Correlation coeff.		
12.5-km resolution									
Rain rate	0.59	0.28	0.27	5.86	4.30	4.27	0.62	0.80	0.80
Convective rain fraction	0.05	0.04	0.03	0.20	0.16	0.16	0.65	0.79	0.79
Integrated latent heating rate	−0.45	−0.68	−0.71	10.60	10.54	10.61	0.63	0.64	0.63
Latent heating rate in layer									
1.0–1.5 km	−0.06	−0.08	−0.07	1.10	1.08	1.06	0.44	0.46	0.50
2.5–3.0 km	−0.05	−0.08	−0.07	1.70	1.70	1.69	0.48	0.47	0.48
4.0–5.0 km	−0.06	−0.09	−0.09	1.69	1.74	1.77	0.57	0.51	0.46
6.0–8.0 km	−0.06	−0.08	−0.08	1.09	1.08	1.14	0.64	0.66	0.58
10.0–14.0 km	0.00	0.00	−0.01	0.26	0.25	0.22	0.72	0.76	0.83
Averaged to 25-km resolution									
Rain rate	0.59	0.28	0.27	3.33	2.25	2.17	0.84	0.92	0.92
Convective rain fraction	0.05	0.04	0.03	0.13	0.10	0.09	0.78	0.88	0.90
Integrated latent heating rate	−0.45	−0.68	−0.71	6.65	6.11	5.61	0.72	0.79	0.84
Latent heating rate in layer									
1.0–1.5 km	−0.06	−0.08	−0.07	0.71	0.69	0.65	0.53	0.58	0.65
2.5–3.0 km	−0.05	−0.08	−0.07	1.14	1.11	1.06	0.56	0.60	0.65
4.0–5.0 km	−0.06	−0.09	−0.09	1.09	1.06	1.03	0.66	0.70	0.72
6.0–8.0 km	−0.06	−0.08	−0.08	0.63	0.58	0.58	0.77	0.82	0.82
10.0–14.0 km	0.00	0.00	−0.01	0.19	0.17	0.13	0.72	0.79	0.91
Averaged to 50-km resolution									
Rain rate	0.59	0.28	0.27	2.22	1.07	1.15	0.93	0.98	0.97
Convective rain fraction	0.05	0.04	0.03	0.09	0.07	0.06	0.86	0.93	0.95
Integrated latent heating rate	−0.45	−0.68	−0.71	4.05	3.50	3.10	0.83	0.90	0.95
Latent heating rate in layer									
1.0–1.5 km	−0.06	−0.08	−0.07	0.36	0.34	0.28	0.76	0.80	0.87
2.5–3.0 km	−0.05	−0.08	−0.07	0.41	0.35	0.33	0.87	0.92	0.93
4.0–5.0 km	−0.06	−0.09	−0.09	0.48	0.43	0.43	0.88	0.94	0.95
6.0–8.0 km	−0.06	−0.08	−0.08	0.43	0.39	0.39	0.84	0.90	0.91
10.0–14.0 km	0.00	0.00	−0.01	0.15	0.12	0.07	0.72	0.80	0.96

timates at 12.5-km resolution over land surfaces; however, correlations with truth are generally lower (Table 2).

Although detailed studies of individual convective systems might require high-resolution estimates of precipitation and latent heating, often storm-average or regional quantities may be sufficient; see Simpson et al. (1988). Therefore, the 12.5-km resolution estimates and truth described previously are area averaged to 25- and 50-km resolution, and statistics of these averaged quantities are computed and presented in Tables 1 and 2. Area averaging does not affect the bias of the estimates, and the reduced error standard deviations of the area-averaged estimates partly reflect the smaller variances of the area-averaged quantities. However, the improved correlations between the area-averaged estimates and truth are significant. For example, the correlation coefficient of the unconstrained rain rate estimates increases from 0.62 (12.5-km resolution) to 0.84 (25-km resolution), and then to 0.93 (50-km resolution) over water surfaces. The correlation coefficients of the convective rain flux fractions and latent heating rates also increase with greater area averaging, and the statistics of algorithm estimates over land follow similar trends. These results reinforce and complement the findings of Kummerow et al. (1996), who noted an increase in the correlations between surface rain rate estimates and truth in synthetic retrievals when the rain rate estimates and truth were area averaged.

Area averaging has another important impact on passive microwave estimates of latent heating rates: if latent heating estimates are area averaged to 25- or 50-km

TABLE 2. Statistics of synthetic retrievals over land surfaces. The three columns under each statistic correspond to estimates using no convective fraction constraint (first column), estimates using a convective fraction constraint on the central grid box only (second column), and estimates using a full convective fraction constraint (third column). Units of bias and error standard deviation are mm h^{-1} (rain rate), kW m^{-2} (vertically integrated latent heating rate), and W m^{-3} (layer-average latent heating rate).

Quantity	Bias			Error std dev			Correlation coeff.		
12.5-km resolution									
Rain rate	1.18	0.71	0.49	5.81	4.68	4.41	0.55	0.75	0.77
Convective rain fraction	0.23	0.19	0.13	0.25	0.21	0.17	0.38	0.64	0.77
Integrated latent heating rate	0.27	−0.13	−0.47	11.67	11.64	11.30	0.60	0.55	0.58
Latent heating rate in layer									
1.0–1.5 km	0.30	0.20	0.09	1.19	1.17	1.11	0.33	0.30	0.44
2.5–3.0 km	0.19	0.09	0.02	1.81	1.84	1.76	0.53	0.30	0.41
4.0–5.0 km	−0.09	−0.11	−0.13	1.84	1.89	1.85	0.50	0.33	0.37
6.0–8.0 km	−0.09	−0.10	−0.10	1.18	1.18	1.20	0.57	0.56	0.52
10.0–14.0 km	−0.02	−0.02	−0.02	0.27	0.26	0.24	0.73	0.78	0.81
Averaged to 25-km resolution									
Rain rate	1.18	0.71	0.49	3.51	2.75	2.29	0.78	0.89	0.91
Convective rain fraction	0.23	0.19	0.13	0.19	0.15	0.10	0.52	0.80	0.91
Integrated latent heating rate	0.27	−0.13	−0.47	7.74	7.30	6.68	0.68	0.74	0.80
Latent heating rate in layer									
1.0–1.5 km	0.30	0.20	0.09	0.82	0.79	0.72	0.28	0.39	0.56
2.5–3.0 km	0.19	0.09	0.02	1.30	1.30	1.22	0.53	0.38	0.49
4.0–5.0 km	−0.09	−0.11	−0.13	1.24	1.24	1.19	0.57	0.52	0.57
6.0–8.0 km	−0.09	−0.10	−0.10	0.69	0.65	0.64	0.75	0.82	0.83
10.0–14.0 km	−0.02	−0.02	−0.02	0.21	0.18	0.15	0.71	0.84	0.90
Averaged to 50-km resolution									
Rain rate	1.18	0.71	0.49	2.66	2.10	1.45	0.90	0.95	0.96
Convective rain fraction	0.23	0.19	0.13	0.16	0.13	0.07	0.66	0.88	0.96
Integrated latent heating rate	0.27	−0.13	−0.47	5.54	4.75	3.80	0.76	0.90	0.97
Latent heating rate in layer									
1.0–1.5 km	0.30	0.20	0.09	0.54	0.47	0.33	0.36	0.80	0.90
2.5–3.0 km	0.19	0.09	0.02	0.72	0.63	0.46	0.82	0.87	0.94
4.0–5.0 km	−0.09	−0.11	−0.13	0.71	0.64	0.56	0.79	0.90	0.94
6.0–8.0 km	−0.09	−0.10	−0.10	0.51	0.45	0.43	0.81	0.91	0.94
10.0–14.0 km	−0.02	−0.02	−0.02	0.15	0.13	0.08	0.71	0.87	0.97

resolution, the correlations between the estimates and truth increase when the convective area fraction constraints are applied. For example, the correlation coefficient of the vertically integrated latent heating rate estimates at 12.5-km resolution over water surfaces remains essentially unchanged after constraints are imposed (see Table 1); however, at 25-km resolution the correlation coefficient increases from 0.72 to 0.79, and finally to 0.84 with the full constraint. At 50-km resolution the correlation coefficient increases from 0.83 to 0.90, and then to 0.95 with the full constraint. The correlation coefficients of the individual layer heating rates respond similarly. Evidently the constraint itself introduces additional random error to the latent heating rate estimates, even though the larger-scale trends in latent heating are better represented. The statistics of latent heating rate estimates over land follow similar trends (Table 2).

The statistics of the synthetic retrievals presented in Tables 1 and 2 quantify algorithm performance under the most ideal conditions. Systematic errors in the cloud–radiative model simulations and sensor observations are not considered in the analysis, and these errors could lead to greater errors in actual remote sensing estimates. Also, the synthetic brightness temperature data are based upon a subset of the cloud/radiative model profiles; the remaining profiles constitute the retrieval algorithm's supporting database. Reasonable algorithm estimates are almost assured, since modeled profiles similar to those observed are likely to be found in the retrieval algorithm's supporting database. However, given the diversity of precipitating weather systems, it is

inevitable that the SSM/I will encounter systems that are very different from the simulated systems that contribute to the supporting database. In these situations the supporting database may not contain simulated profiles that are radiatively consistent with the SSM/I observations, and greater errors are expected.

Nevertheless, the foregoing analysis suggests that even under ideal conditions, supplemental information regarding the areal fraction of convection is needed to obtain reliable estimates of rainfall rate and convective rain flux over water surfaces. In addition, retrieved latent heating rates must be averaged over relatively large areas (25 km × 25 km or more) to obtain useful estimates. Estimates of surface rain rate, convective area fraction, and latent heating rates over land surfaces have greater uncertainty than those over water backgrounds.

5. SSM/I applications

a. Specification of the convective area fraction constraint

In the applications that follow, the retrieval algorithm is applied to SSM/I observations of precipitation systems over the tropical/subtropical oceans. In section 4, it was demonstrated that unambiguous SSM/I estimates of rain rate, convective rain flux fraction, and latent heating rates required information regarding the areal fraction of convection within a nominal footprint in addition to the coincident brightness temperature observations. Hong et al. (1999) tested several indices, derived from passive microwave brightness temperature measurements, for separating convective and stratiform rain areas. In their study an index was developed that combined the depression at 85.5 GHz with respect to the clear-air background brightness temperatures and the local maximum depression of 85.5-GHz brightness temperature with respect to any of the neighboring 85.5-GHz measurements in the SSM/I swath. Formally,

$$\mathrm{CSI} = (\mathrm{TB85h}_{\mathrm{clr}} - \mathrm{TB85h}) + \max_i(\mathrm{TB85h}_i - \mathrm{TB85h}), \qquad (15)$$

where TB85h and $\mathrm{TB85h}_{\mathrm{clr}}$ are the brightness temperature and background clear-air brightness temperature, respectively, at 85.5 GHz in the horizontal polarization. The term $\mathrm{TB85h}_i$ indicates any of the eight SSM/I brightness temperatures surrounding the central measurement, TB85h. Also, it is understood that the expression $\mathrm{TB85h}_{\mathrm{clr}} - \mathrm{TB85h}$ is zero unless $\mathrm{TB85h}_{\mathrm{clr}}$ exceeds TB85h, and that $\mathrm{TB85h}_i - \mathrm{TB85h}$ is zero unless $\mathrm{TB85h}_i$ exceeds TB85h for some *i*. The rationale for the index is that large 85.5-GHz brightness temperature depressions, especially those associated with substantial gradients of brightness temperature, are indicative of scattering by relatively dense, precipitation-sized ice hydrometeors, and these hydrometeors are generally formed within or near the stronger updrafts of convective systems. Hong et al. (1999) related the index (15) to the areal fraction of convective rainfall by matching the cumulative distributions of convective area fractions derived from COARE shipboard radar data and synthesized SSM/I CSI measurements. This probability matching approach was utilized since any small spatial misregistration of the two datasets could lead to low correlations between the convective fraction and CSI. The resulting empirical relationship is well approximated by

$$f_{AO} = \begin{cases} 0, & \mathrm{CSI} < 25 \\ (7.752 \times 10^{-3})(\mathrm{CSI} - 25), & 25 \le \mathrm{CSI} \le 154 \\ 1, & \mathrm{CSI} > 154. \end{cases} \qquad (16)$$

An alternative relationship, developed in the present study, is based upon analyses of SSM/I observations by Spencer et al. (1989) and Heymsfield and Fulton (1994a,b). These authors found significant differences, on the order of 5 K or greater, between the vertically and horizontally polarized 85.5-GHz brightness temperatures in stratiform rain regions over land, whereas regions of strong convection were nearly unpolarized at 85.5 GHz. Although the physical basis of these polarization differences has not been verified, the aforementioned authors hypothesized that precipitation-sized ice particles such as snow or aggregates would tend to become oriented as they fall through the relatively weak updrafts or downdrafts of stratiform rain regions, resulting in preferential scattering in the horizontal polarization. The more turbulent, vigorous updrafts of convective regions would cause ice hydrometeors to lose any preferred orientation, leading to similar scattering signatures in both polarizations. Recently, Petty and Turk (1996) and Schols et al. (1997) performed microwave radiative transfer calculations through clouds of oriented, aspherical ice hydrometeors and found polarization differences exceeding 5 K, supporting this hypothesis.

In the present study, the ''normalized polarization difference'' of Petty (1994) is used as a measure of polarization at 85.5 GHz,

$$\mathrm{P85} = \frac{\mathrm{TB85v} - \mathrm{TB85h}}{[\mathrm{TB85v} - \mathrm{TB85h}]_{\mathrm{clr}}}. \qquad (17)$$

The denominator on the right-hand side of (17) is the difference between the vertically and horizontally polarized 85.5-GHz brightness temperatures in clear conditions. Over water surfaces, the clear-air polarization difference is sampled from a 3 × 3 neighborhood of 85.5-GHz brightness temperature measurements; the polarization differences of measurements that have liquid water paths less than 0.01 kg m^{-2} according to the method of Karstens et al. (1994) are averaged to obtain the clear-air difference in (17). If no clear-air measurements are found in a given 3 × 3 neighborhood, then the last

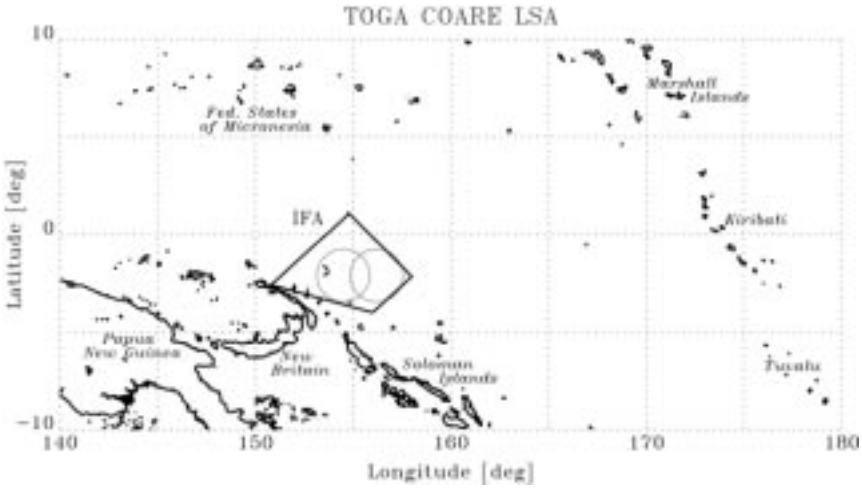

FIG. 7. Map of the TOGA COARE Large Scale Array, with the Intensive Flux Array polygon (heavy solid lines) and shipboard radar domains (thin solid lines) indicated.

valid clear-air polarization difference calculated from the SSM/I data over a water surface is substituted.

Given the definition (17), the quantity 1 − P85 may be interpreted physically as the unpolarized fraction of the 85.5-GHz footprint. If convective regions are largely unpolarized at 85.5 GHz, and stratiform or cloud-free regions (over water surfaces) have some degree of polarization, then it follows that 1 − P85 should be roughly proportional to the convective area fraction. Analysis of collocated SSM/I 85.5-GHz observations and TOGA COARE shipboard radar observations indicate a 0.4 offset that optimizes the fit between the cumulative distributions of convective area fraction deduced from the shipboard radars and the cumulative distributions of 1 − P85:

$$f_{AO} = (1 - \mathrm{P85}) - 0.4. \tag{18}$$

Over land surfaces, the clear-air polarization difference is generally less than 5 K; therefore, to distinguish regions of low polarization from convective regions, rain-covered footprints are first identified using the screening software developed by Adler et al. (1994) and Huffman et al. (1995). Then, in SSM/I footprints containing significant rain, a clear-air polarization difference of 12 K is prescribed in (17) to force P85 to respond to convective rain area fraction in a manner similar to the way it responds over ocean. The convective area fraction is again computed using (18).

Although approximate, SSM/I-based estimates of the convective area fraction given by (16) and (18) are introduced to assess the impact of convective–stratiform rain classification on the microwave remote sensing of rain rates, convective rain flux fractions, and latent heating profiles. Both estimates of convective area fraction are calibrated using TOGA COARE radar data that are classified using the method of Short et al. (1997). It is expected that data from the higher-resolution TRMM Microwave Imager and/or Precipitation Radar will lead to improved methods for inferring convective area fraction; see Hong et al. (1999).

b. TOGA COARE

TOGA COARE was designed to study the principal processes responsible for the coupling of the ocean and atmosphere in the western Pacific warm-pool region (Webster and Lukas 1992). To this end, observations from ship, buoy, aircraft, rawinsonde, and satellite platforms were collected during the COARE Intensive Observing Period (IOP) from 1 November 1992 to 28 February 1993. Rawinsonde temperature, humidity, height, and wind data were obtained from 30 sites over the Large Scale Array (LSA), with a concentration of sites surrounding the Intensive Flux Array (IFA); see Fig. 7. Surface observations of SST, temperature, humidity, pressure, and winds were collected from ships and buoys, also in proximity of the IFA. The Massachusetts Institute of Technology (MIT) and NOAA/TOGA 5-cm radars were operating continuously from shipboard platforms within the IFA, providing volumetric scans out to 150-km range. Areas of radar coverage associated with nominal ship locations are depicted in Fig. 7. During the COARE IOP, SSM/Is were operating on two of the Defense Meteorological Satellite Program satellites,

→

FIG. 8. Estimated surface rain rates (left column) and convective rain rates (right column) at 1101 UTC 20 Dec 1992 from the SSM/I retrieval method with the C1 constraint (top row) and C2 constraint (middle row), and from the MIT radar (bottom row). The limit of radar coverage is indicated by a white circle superimposed on the SSM/I rain patterns. Island coastlines are also indicated in white.

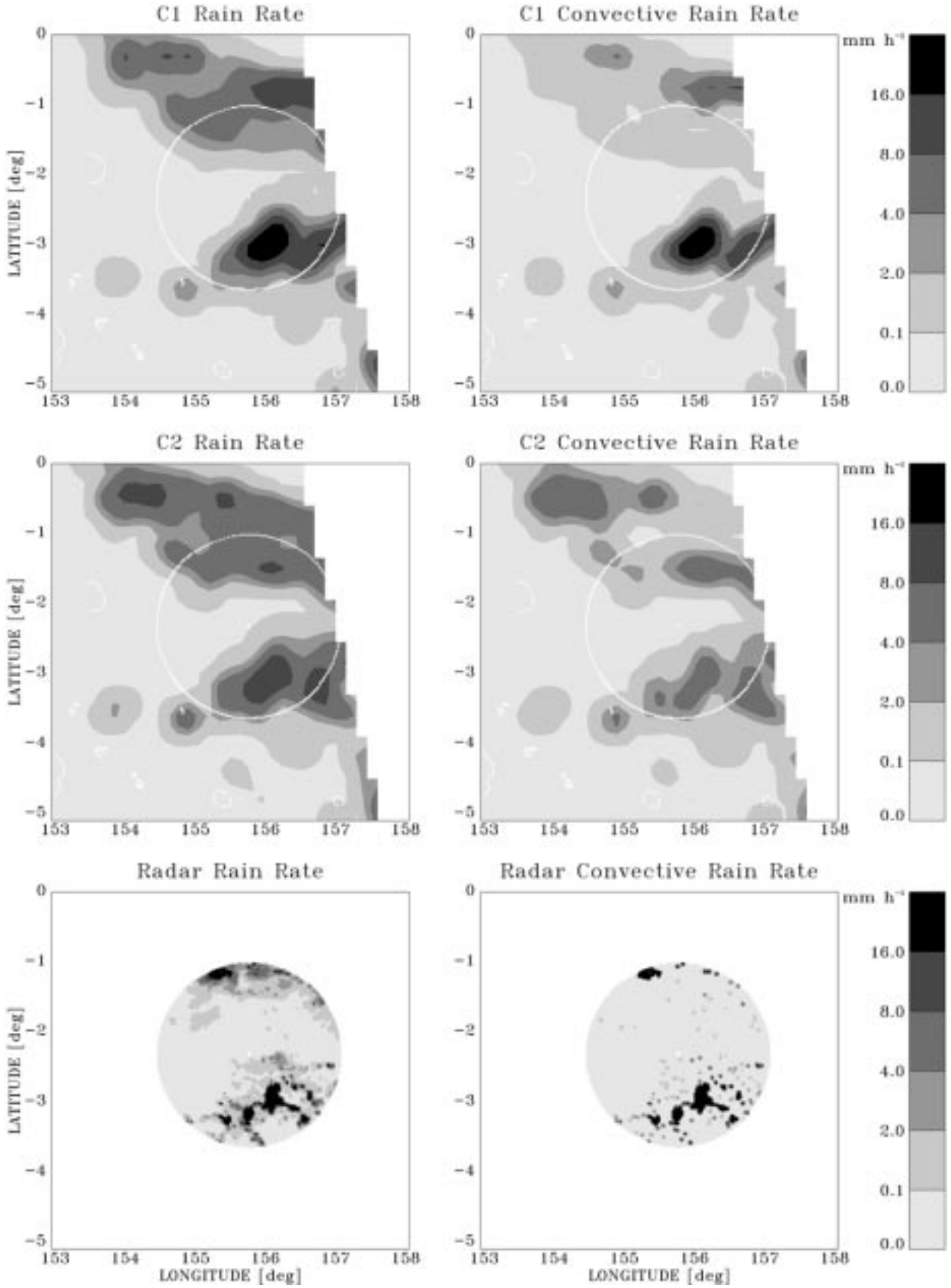
C1 Rain Rate
C1 Convective Rain Rate
C2 Rain Rate
C2 Convective Rain Rate
Radar Rain Rate
Radar Convective Rain Rate
LATITUDE [deg]
LONGITUDE [deg]
mm h⁻¹
16.0
8.0
4.0
2.0
0.1
0.0
0
−1
−2
−3
−4
−5
153
154
155
156
157
158

DMSP-F10 and *-F11*, providing at least partial coverage of the LSA about 4 times per day. *DMSP-F10* traversed the IFA at roughly 0830 LT and 2030 LT, while *DMSP-F11* made its traverse at about 0500 and 1700 LT.

The retrieval algorithm (12), both unconstrained and constrained by estimates of the convective area fraction from 85.5-GHz scattering signatures [Eq. (16), hereafter C1] or polarization signatures [Eq. (18), hereafter C2], is applied to SSM/I observations within the COARE LSA over the entire IOP. Examples of retrieved precipitation fields from specific SSM/I overpasses of the COARE IFA are presented in Figs. 8 and 9. The SSM/I and MIT radar observations at 1101 UTC on 20 December 1992 are shown in Fig. 8, while observations from the SSM/I and combined MIT–NOAA/TOGA radars at 1031 UTC on 24 December 1992 are displayed in Fig. 9. Both sets of observations come from the 2-week period of active convection preceding the peak of low-level westerly winds on 1 January 1993 (Lin and Johnson 1996). In both figures, panels in the top row depict SSM/I surface precipitation fields retrieved using C1. The middle row panels are the same fields retrieved using C2, while the bottom row panels are derived from the IFA radars. Note that the SSM/I rain rates have been contoured from retrievals averaged over 25 km $\times$ 25 km areas, following the analysis of section 4, which indicated a significant reduction of random errors in retrieved precipitation and latent heating fields that had been area averaged in this way. Convective rain rates from the SSM/I are computed by multiplying the retrieved rain rate R by the retrieved convective rain flux fraction, f_R. The radar rain rates are derived from low-level reflectivity data and analyzed on a 2-km resolution grid by the National Aeronautics and Space Administration's TRMM Office, using an adaptation of the Tao et al. (1993a) method as described in Short et al. (1997). Radar rain rates are classified as either convective or stratiform at grid resolution; therefore, the radar convective rain field comprises only rain intensities at convective grid points. Listed in Table 3 are the bivariate statistics of coincident pairs of instantaneous SSM/I and radar rain rate estimates area averaged over 0.5° $\times$ 0.5° boxes. All coincident pairs within 100 km of one of the shipboard radars are included in the statistics.

It may be noted from Figs. 8 and 9 that although the SSM/I rain patterns are correlated with the radar-derived patterns, there is a general tendency for both the C1 and C2 SSM/I algorithms to yield rain rates that are high-biased with respect to the radar estimates, especially in the range of low to moderate rain rates (0.1–16 mm h^{-1}). This tendency is reflected in the IOP bias statistics of Table 3. Note, however, that the high bias of either the C1 or C2 constrained SSM/I estimates is smaller than the bias of the unconstrained estimates. On the other hand, the bias of retrieved *convective* rain rates is relatively small, which suggests that a high bias in retrieved stratiform rain rates is the main contributor to the total bias. Comparisons of fields of unconstrained SSM/I rain estimates (not shown) to radar-derived rain fields indicate a substantial high bias of the unconstrained estimates in stratiform rain regions, which typically cover a large percentage of the raining area. As anticipated from the analysis in section 2c (see Fig. 3), the added constraints help to lower the rain rate estimates in the stratiform regions, thereby reducing the overall mean rain rate. Rain rate estimates in convective regions are somewhat enhanced by the constraints, and the combination of lighter stratiform rains and more intense convective rains leads to a greater convective rain flux percentage overall.

The C1 algorithm utilizes ice–precipitation scattering signatures to identify regions of strong updraft and convective rainfall. This constraint works well in regions where higher ice concentrations are associated with convection, as in the large convective zone near 3°S, 156°E on 20 December 1992 (see Fig. 8). However, sometimes substantial ice concentrations that produce 85.5-GHz scattering signatures less than 220 K may occur in stratiform rain regions; see Spencer et al. (1989) and Heymsfield and Fulton (1994a,b). For example, the convective rain maximum retrieved using C1 near 2°S, 154°E on 24 December 1992 (Fig. 9) is associated with 85.5-GHz horizontal brightness temperatures near 210 K, but only small convective cells are identified by the radar. In addition, tropical convection may be shallow or strongly sheared, producing very little precipitating ice. The convective line near 1.5°S between 154°E and 155.5°E on 24 December 1992 (Fig. 9) produces a scattering depression of only 250 K, and therefore the C1 algorithm does not indicate significant convection. In these situations the 85.5-GHz polarization signature may be useful for distinguishing convective and stratiform precipitation areas. At 2°S, 154°E on 24 December 1992 the C2 algorithm yields primarily stratiform rain, in spite of the scattering signature at 85.5 GHz, and along the convective line near 1.5°S between 154°E and 155.5°E on 24 December 1992, C2 correctly assigns significant convective rainfall. Statistically, the C2 algorithm yields rain rate estimates with lower random error and a higher correlation with radar estimates. Overall, C2 estimates of *convective* rain rates are high-biased and have greater random error than the unconstrained estimates, but the correlation of C2 convective rain rates with radar is significantly greater than the correlations of the other estimates with radar.

In Fig. 10, plan views of the C2 retrieved vertically integrated latent heating rate, and the latent heating rates at the 3- and 7-km levels from the 1101 UTC 20 December 1992 and 1031 UTC 24 December 1992 SSM/I overpasses are presented in the left and right columns, respectively. In general, the patterns of vertically integrated latent heating follow the surface precipitation patterns (see Figs. 8 and 9), which is expected from the perspective of moisture conservation [Eq. (4)]. At the 3-km level, positive latent heating rates are retrieved in regions dominated by convective precipitation, while

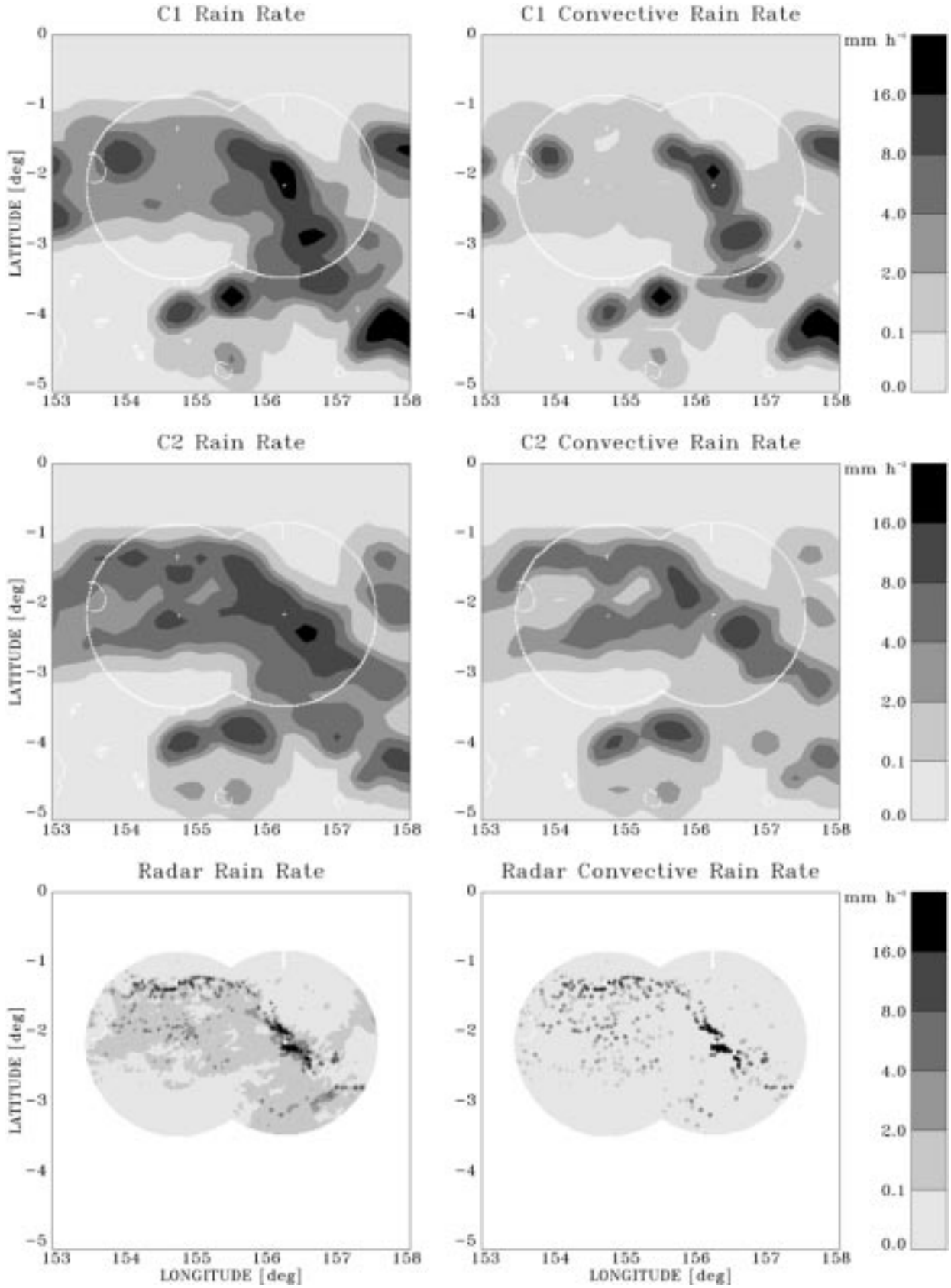

FIG. 9. Like Fig. 8 but at 1031 UTC 24 Dec 1992 and with rain rates from the combined MIT–NOAA/TOGA radars in the bottom row.

TABLE 3. Statistics of SSM/I estimates of rain rates over the TOGA COARE IFA. The three columns under each statistic correspond to estimates using no convective fraction constraint (first column), estimates using the C1 convective fraction constraint (second column), and estimates using the C2 convective fraction constraint (third column). Units of bias and error standard deviation are mm h^{-1}.

Quantity	Bias			Error std dev			Correlation coeff.		
Rain rate	0.23	0.16	0.21	1.38	1.22	1.14	0.61	0.63	0.68
Convective rain rate	−0.01	0.00	0.09	0.63	0.85	0.78	0.44	0.40	0.58

evaporative cooling occurs in stratiform rain regions. On 24 December 1992, the leading edge of convection along a line between (roughly) 1°S, 155°E and 3°S, 158°E was propagating to the ENE. Low-level heating predominates along this line, while following the line, a mixture of evaporative cooling and weak heating occurs in the trailing stratiform region. At the 7-km level, relatively weak but positive latent heating dominates the heating patterns. Although latent heating maxima at 7 km sometimes coincide with strong convection (e.g., near 3°S, 156°E on 20 Dec 1992), significant heating may also occur in stratiform regions, or regions overlying low-level evaporative cooling. For example, on 24 December 1992 latent heating maxima are retrieved south and west of the leading edge convection where cooling at lower levels is observed. It has been noted that upper-level heating and low-level cooling are characteristic of the stratiform regions of squall lines; see section 2a.

The SSM/I C2 estimates of surface rain rate, convective rain rate, and latent heating are composited at 1° × 1° resolution from all *F10* and *F11* overpasses of the COARE LSA during the 4-month IOP. Presented in Fig. 11 are the SSM/I IOP-mean rain rates, as well as the IOP-mean rain rates from the moisture budget analysis of Lin and Johnson (1996, hereafter LJ) and from European Centre for Medium-Range Weather Forecasts (ECMWF) model forecasts. The overall pattern of SSM/I estimates appears to be most consistent with the ECMWF estimates, although a significant low bias of SSM/I rain rates over land regions is apparent. The low bias is attributed to the relative lack of precipitation signal over high-emissivity land backgrounds; therefore, over land the retrieved rain rates tend toward the mean rain rate of the supporting cloud model database, which is relatively low. This behavior of the retrieval algorithm was previously described in Olson et al. (1996). Nevertheless, evidence of a double ITCZ precipitation pattern, with zonally oriented rain maxima above and below the equator west of 170°E and a relative minimum of rainfall near the equator, is provided by the SSM/I and ECMWF composite rain maps.

The moisture budget estimates of surface rain rate were computed as the sum of the rawinsonde-derived, vertically integrated total atmospheric moisture sink (Q_2) and estimates of surface evaporation from buoy-adjusted ECMWF analyses by LJ. The budget estimates of IOP-mean rainfall rates are in reasonable agreement with the ECMWF rain rates and SSM/I estimates (over ocean) in the central and western portions of the LSA, where rawinsonde stations were more numerous and surface evaporation estimates were more reliable; see LJ.

Over the IFA, the SSM/I, moisture budget, and ECMWF IOP-mean rain rate estimates are 8.7, 5.6, and 9.1 mm day^{-1}, respectively. These estimates may be compared to the IOP-mean shipboard radar estimate of 4.9 mm day^{-1}. Although these estimates cover a substantial range, differences in the spatial coverage and temporal sampling, in addition to the intrinsic uncertainty in each rain estimate, could account for biases in the IOP-mean estimates. For example, the SSM/I, moisture budget, and ECMWF estimates represent the mean values of rain rate over the entire IFA polygon. In contrast, the radar estimate is based upon measurements only within 150 km of the shipboard radar sites (see Fig. 7), and so the entire IFA is not sampled. Since the radars observe primarily the central and eastern portions of the IFA, where mean rain rates tend to be greater than in the north and west (Fig. 11), the IOP-mean shipboard radar estimate is likely greater than that which would be obtained from uniform IFA coverage. Regarding time sampling, the mean diurnal cycle of rainfall was estimated from the shipboard radars in the IFA by Short et al. (1997). The 0500 LT SSM/I overpass occurred within the early morning relative maximum of rainfall, while the 0830 LT and 1700 LT overpasses occurred within the broad daytime relative minimum, and the rain rate at 2030 LT was approximately equal to the daily mean. If the shipboard radar observations are sampled only at the four SSM/I overpass times during the entire IOP, then the IOP-mean rain rate computed from these samples is very close to the daily mean of all radar observations. This fortuitous result implies that the SSM/I undersampling of the diurnal cycle should not have a great impact on SSM/I IOP-mean rain es-

→

FIG. 10. Estimated vertically integrated latent heating rates (top row) and latent heating rates near 3 (middle row) and 7 km (bottom row) from the SSM/I retrieval method with the C2 constraint. Estimates from observations at 1101 UTC 20 Dec 1992 and at 1031 UTC 24 Dec 1992 are in the left and right columns, respectively. Coastlines have been removed for clarity.

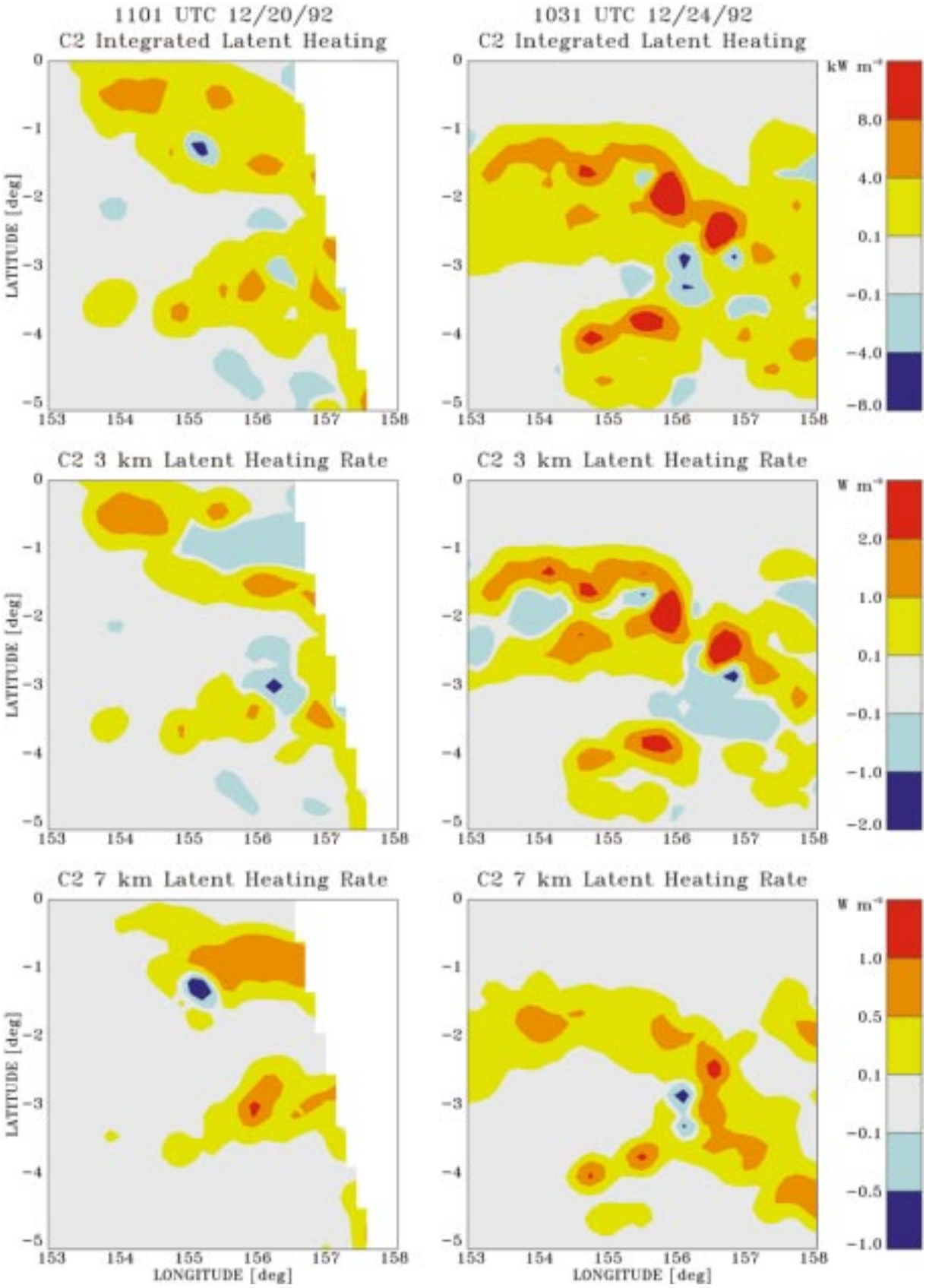
1101 UTC 12/20/92
C2 Integrated Latent Heating
1031 UTC 12/24/92
C2 Integrated Latent Heating
kW m⁻²
8.0
4.0
0.1
−0.1
−4.0
−8.0
C2 3 km Latent Heating Rate
C2 3 km Latent Heating Rate
W m⁻²
2.0
1.0
0.1
−0.1
−1.0
−2.0
C2 7 km Latent Heating Rate
C2 7 km Latent Heating Rate
W m⁻²
1.0
0.5
0.1
−0.1
−0.5
−1.0
LATITUDE [deg]
LONGITUDE [deg]
0
−1
−2
−3
−4
−5
153
154
155
156
157
158

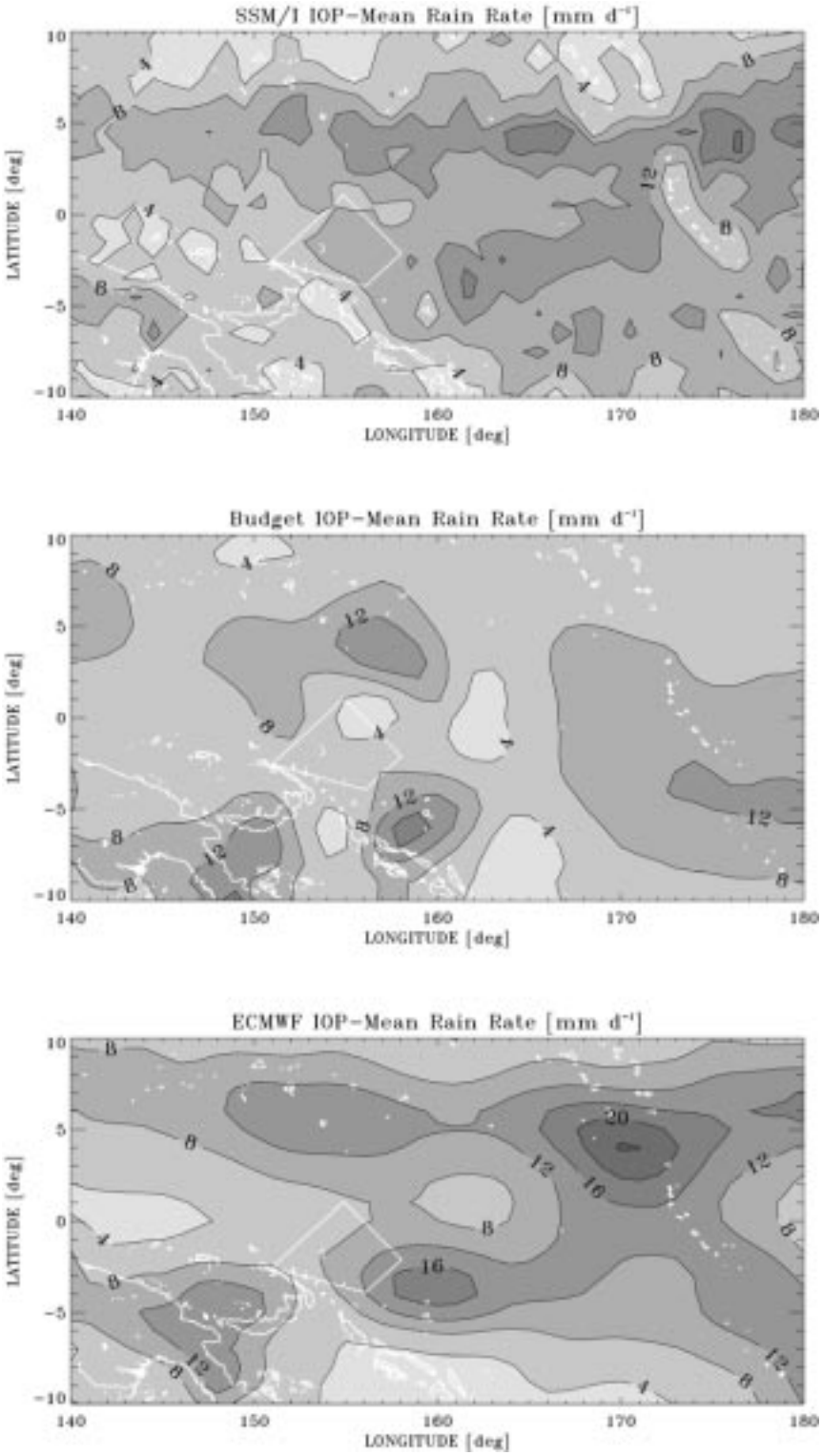

FIG. 11. IOP-mean rain rates over the TOGA COARE LSA from the SSM/I retrieval method with the C2 constraint (top), moisture budget (middle; from Lin and Johnson 1996), and ECMWF forecasts (bottom; from Lin and Johnson 1996). IFA boundaries and coastlines are indicated in white.

timates over the IFA. It may be concluded that there are still large *intrinsic* differences in the IOP-mean IFA rain estimates from the four methods: SSM/I and ECMWF estimates are significantly greater than the moisture budget and radar estimates.

Presented in Fig. 12 are the fields of IOP-mean convective rain flux percentage, vertically integrated latent heating rate, and level of maximum latent heating estimated using the SSM/I C2 algorithm. The convective rain flux percentages vary from about 50% to 65% over the LSA, with a slight tendency for lower percentages along the ITCZ bands and higher percentages over land and over lightly raining areas over ocean. A greater percentage of stratiform precipitation in the ITCZ suggests that more organized mesoscale convective systems contribute to rainfall in these bands. This interpretation is supported by the finding of Rickenbach and Rutledge (1998), who noted that mesoscale convective systems with a length scale greater than 100 km contributed to 85% of the IFA rainfall during the COARE IOP.

The pattern of vertically integrated latent heating closely follows the pattern of surface rain rates shown in Fig. 11. However, the latent heating relative maximum over Papua New Guinea is more prominent than the coincident maximum of rain rate. This result is consistent with the greater percentage of convective rainfall over Papua New Guinea: simulations of evolving mesoscale convective systems using the GCE model exhibit an initial phase dominated by convection, where the net condensation of water vapor in the atmosphere exceeds the rate of precipitation fallout. Therefore, in this phase the vertically integrated latent heating rate exceeds the rainfall equivalent energy flux, $\rho_l L_v R$; see (4). As the system matures, the percentage of stratiform precipitation increases markedly, and eventually the rate of precipitation fallout surpasses the net condensation of water vapor in the atmosphere. The rainfall equivalent energy flux then becomes greater than the vertically integrated latent heating. Since the IOP-mean convective rainfall percentage exceeds 65% over Papua New Guinea, convective processes dominate, and the net condensation/latent heating in the atmosphere is slightly greater than what might be inferred from the surface rain rate and simple moisture balance.

Displayed in the final panel of Fig. 12 is the estimated level of maximum latent heating over the LSA. In determining the level of maximum heating, the vertical profiles of latent heating are first converted to equivalent profiles of heating rate per unit mass using the IFA mean sounding from X. Lin and R. Johnson 1997 (personal communication). The levels of maximum heating rate are then contoured to produce the figure. Over the ocean, the heights of the maximum heating rate are weakly anticorrelated with the convective rainfall percentage. This result is consistent with model simulations (e.g., Fig. 1), and observational evidence (see Houze 1989), which indicate a low- to midtropospheric maximum of vertical motion and latent heating in areas of convection, and upper-tropospheric mesoscale lifting (heating) and lower-tropospheric downdrafts (cooling) in stratiform regions. Over Papua New Guinea, though, it appears that more vigorous convection contributes to a deep layer of lifting and heating, with a maximum of latent heating near 5.5-km altitude. Retrieved profiles of latent heating over land should be regarded with caution, however, since the signal of precipitation in the SSM/I measurements is partly obscured by the high-emissivity land backgrounds.

A time series of daily SSM/I (C2 algorithm) latent heating profiles over the IFA during December 1992 is presented in Fig. 13. Rawinsonde-derived Q_1 profiles over the IFA have been calculated by LJ and Frank et al. (1996), and the profiles of LJ are presented in Fig. 13 for comparison. Although the apparent heat source, Q_1 includes radiative heating/cooling and sensible heat flux convergence/divergence in addition to latent heating, these additional contributions are expected to be relatively small. There is a general correspondence between heating and cooling features in the SSM/I and rawinsonde-derived time series; however, the comparison suggests a low bias in the altitude of the maximum heating as well as excessive low-level cooling in the SSM/I profiles. These biases are reflected in the IOP-mean profiles shown in Fig. 14, in which both the latent heating and Q_1 profiles have been normalized by the estimated IOP-mean precipitation rate to emphasize differences in profile shape, rather than differences in integrated heating. Differences in the phase and magnitude of heating/cooling features in the two heating profile time series in Fig. 13 may be partly attributed to the different sampling of the SSM/I and rawinsonde observations. Since the two SSM/Is together may overpass the IFA as little as one time per day, the time series of latent heating exhibits greater magnitude fluctuations than the Q_1 time series, which is based upon 6-hourly rawinsonde data.

The apparent deficiency in upper-level heating from SSM/I might be explained by a lack of signal in SSM/I measurements from tenuous anvil cloud, which may yet contribute to heating aloft. For example, in the simulated squall line depicted in Figs. 1 and 2, positive latent heating between 6- and 12-km altitude is evident in the stratiform anvil rearward of $X = 150$ km, in the cross section at $Y = 210$ km (Fig. 1b). Note, however, that there is relatively little microwave signal from this portion of the squall line, either in the emission at 19.35 GHz (Fig. 2c) or in the scattering depression at 85.5 GHz (Fig. 2d). In addition, the low-resolution emission channels of SSM/I may not be able to detect small, shallow convective cells, which could explain the slight cooling below 900 mb in the mean latent heating profile. Nevertheless, it is encouraging that the retrieved horizontal distributions of rain rate, convective fraction, integrated latent heating, and level of maximum heating appear to be consistent. Improvements in sensor resolution, which may increase the absolute accuracy of

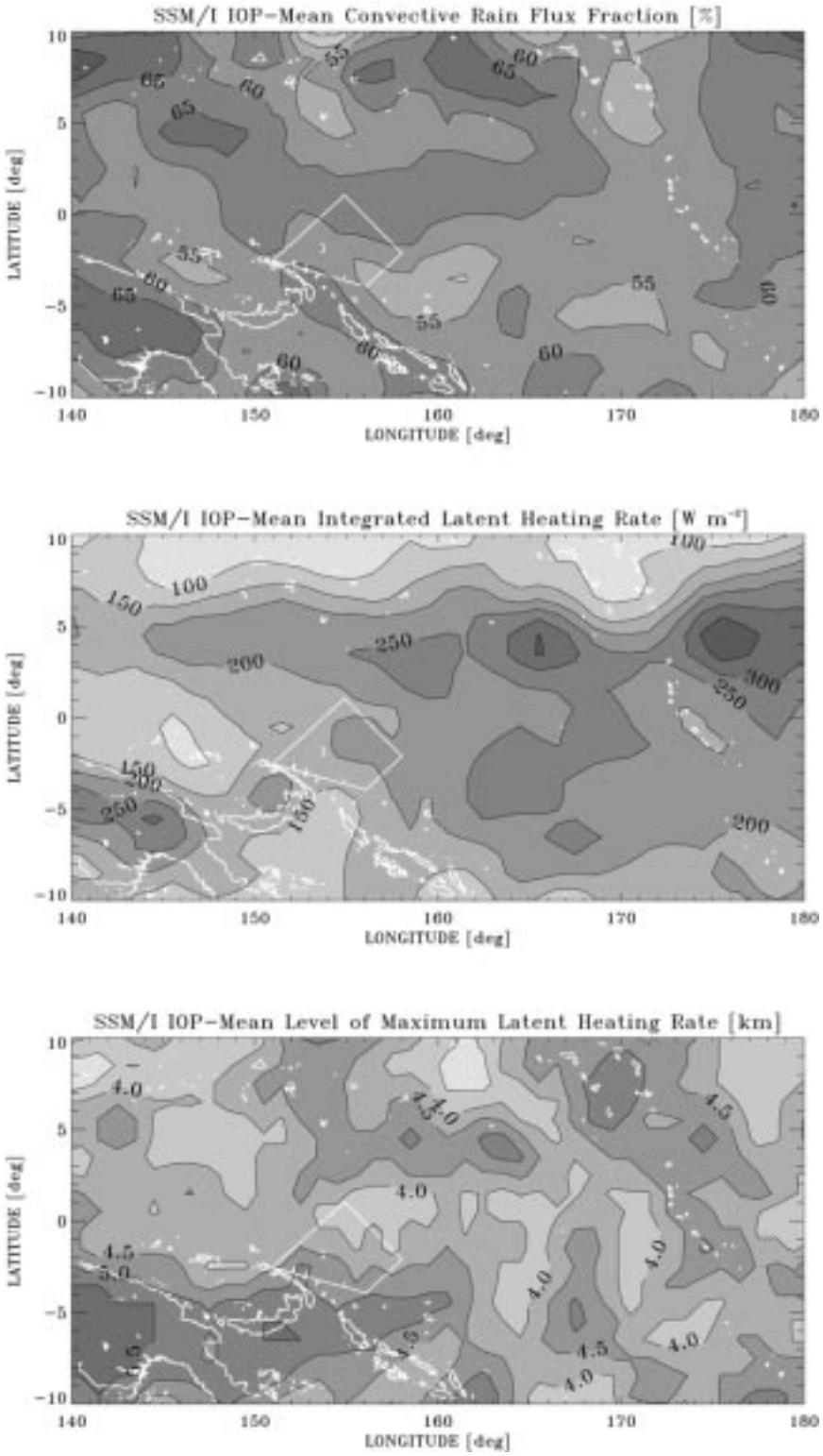

FIG. 12. IOP-mean convective rain flux fraction (top), vertically integrated latent heating rate (middle), and level of maximum latent heating rate (bottom) over the TOGA COARE LSA, estimated using the SSM/I retrieval method with the C2 constraint. IFA boundaries and coastlines are indicated in white.

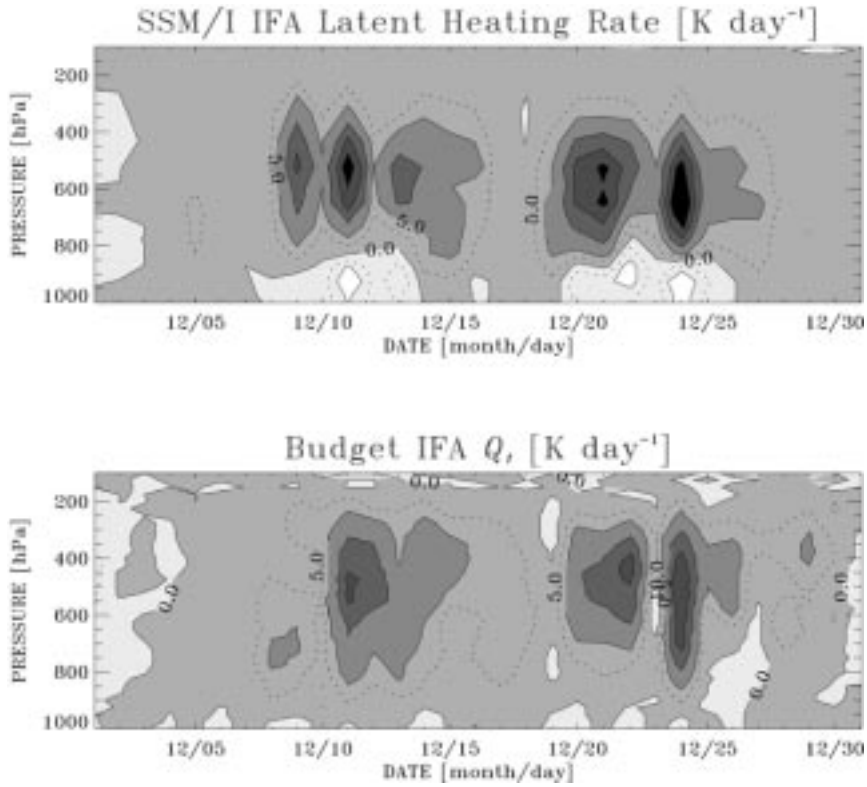

FIG. 13. Time series of daily SSM/I latent heating profiles over the TOGA COARE IFA (upper panel) and daily apparent heat source (Q_1) profile over the IFA from rawinsonde analyses (lower panel; from Lin and Johnson 1996) during Dec 1992. Contour interval is 5 K day^{-1}.

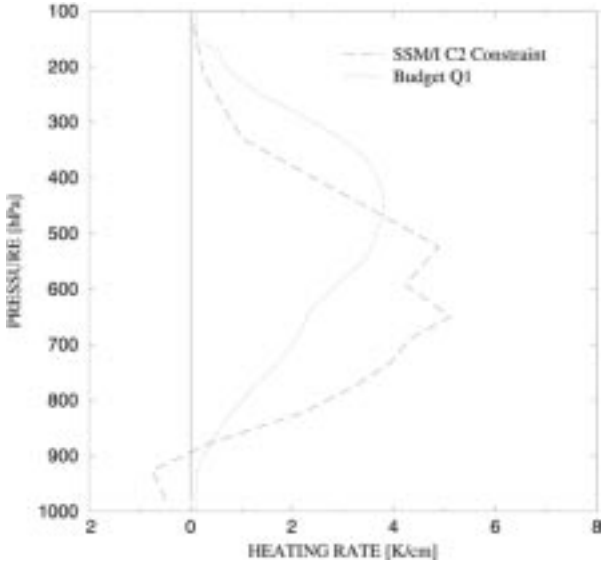

FIG. 14. IOP-mean latent heating rate profile over the TOGA COARE IFA, estimated using the SSM/I retrieval method with the C2 constraint (long-dashed line). Also plotted is the IOP-mean apparent heat source (Q_1) profile over the IFA from rawinsonde analyses (dotted line; from Lin and Johnson 1996).

retrieved profiles, are expected in forthcoming satellite missions.

c. Hurricane

In tropical cyclones, the relationship between storm intensity and the distribution of precipitation/latent heating has been the subject of considerable study, both from theoretical and observational perspectives (e.g., Eliassen 1952; Schubert and Hack 1982; Shapiro and Willoughby 1982; Marks 1985; Willoughby 1990). Observational evidence supports the idea that the latent heat released in convective ''rings'' centered on the tropical cyclone vortex leads to descent, adiabatic warming, and pressure falls within the area the ring encloses (Willoughby et al. 1982; Willoughby 1990; Black and Willoughby 1992). Satellite passive microwave radiometry has been used to estimate the total rainfall and associated latent heat release within the inner core regions of tropical cyclones by Rodgers and Adler (1981), Rodgers et al. (1994), and Rodgers and Pierce (1995). These studies have revealed increases in tropical cyclone maximum wind speed correlated with increases in inner core precipitation/latent heating, although the temporal sampling of the precipitation by the polar-orbiting sensor platforms was limited to one to two observations per day in the early studies. Since 1992, at least two SSM/I

sensors have been operational on DMSP satellites, and new instruments such as the TMI and the AMSR will help to increase the frequency of tropical cyclone observations. As temporal sampling has improved, tracking the evolution of tropical cyclone precipitation/latent heating distributions by passive microwave radiometry has become more feasible, and therefore studies of the physical processes linked to storm intensification have been enhanced.

In the aforementioned studies, microwave-based estimates of latent heating distributions were inferred from estimates of surface rain rates using the moisture balance relationship (4). Estimates of latent heating distributions in tropical cyclones based upon a combination of passive microwave data and cloud-resolving models have also been attempted; see Tao et al. (1993b), Smith et al. (1994), and Raymond et al. (1995). In these more recent studies, surface rain rates and/or hydrometeor profiles were first retrieved from SSM/I observations, and latent heating profiles consistent with the retrieved parameters were then calculated. In the current study, physically consistent latent heating profiles are computed as an integral part of the retrieval process, as described in section 3.

The SSM/I C1 and C2 retrieval algorithms are applied to *DMSP-F10* and *-F11* SSM/I observations of Hurricane Andrew, following its passage over the Florida peninsula on 24 August 1992. Surface rain rates and convective rain rates retrieved from SSM/I observations at 2259 UTC on 24 August 1992, as Andrew made its landfall on the Louisiana coast, are displayed in Fig. 15 along with coincident rain rate estimates from the WSR-57, 10-cm radar at Slidell, Louisiana. Gridded radar reflectivities at 2-km resolution from the lowest elevation-angle (0.4°) plan position indicator (PPI) scan are converted to rain rate using the ''Miami'' relationship [$Z = 300R^{1.4}$; Woodley (1970)]. The method of Short et al. (1997) is applied to the radar rain rate data to classify convective and stratiform regions. The C1 and C2 retrieved rain rate distributions are similar, although the convective rainbands over land in the C1 retrieval are more intense. Both versions of the algorithm yield extensive stratiform precipitation mainly over the Gulf of Mexico to the southwest of the radar site, in agreement with the radar observations. The primary differences in the retrieved precipitation patterns are the eyewall convection identified by C1 but not C2, and the much greater proportion of convective precipitation in the C2 rain estimates within the outer rainband to the southwest of the eye. The radar classification method also fails to identify convective precipitation in the eyewall, although the maximum rain rate in the northwest portion of the eyewall (21 mm h^{-1}) is close to the convective rain threshold of 22 mm h^{-1} in the classification method. Rain estimates within the outer rainband are beyond the range of the radar, and therefore they cannot be verified.

Although the two algorithm constraints lead to different retrieved rainfall patterns in Andrew, the C2 estimates were previously shown to be in better agreement with COARE radar observations, and the latent heating patterns obtained with the C2 version exhibit greater coherence and consistency with conceptual models of mesoscale convective system structure. Actual validation of latent heating estimates in climatologically dissimilar regions will be the subject of a future study. Notwithstanding, the potential of microwave radiometry in estimating latent heating distributions is illustrated by the application of the retrieval algorithm (C2 constraint) to a sequence of SSM/I observations of Hurricane Andrew. In Figs. 16a–d are plan views of the retrieved vertically integrated latent heating rates, and the retrieved latent heating rates at the 3- and 7-km levels from SSM/I observations of Andrew at 1448 UTC on 24 August 1992, and at 0156, 1140, and 2259 UTC on 25 August 1992. During the time period spanned by these observations, Andrew's central pressure is estimated to have dropped from 951 hPa at 1200 UTC on 24 August to 937 hPa at 0000 UTC on 26 August, and Andrew's estimated maximum surface wind speed increased from 56.7 m s^{-1} to 61.9 m s^{-1} [pressure and wind estimates from National Hurricane Center best track; Mayfield et al. (1994)]. These estimates indicate a period of moderate intensification.

At 1448 UTC on 24 August, Andrew's eye was located just off the west coast of Florida, and although the pattern of vertically integrated latent heating from SSM/I is fairly axisymmetric (see Fig. 16a), the pattern of upper-level heating and coincident radar observations from Tampa Bay (not shown) reveal somewhat asymmetric structure, with a large outer band extending over the Florida peninsula. Later, at 0156 UTC on 25 August, the storm had moved westward over the Gulf of Mexico and exhibited more axisymmetric structure (Fig. 16b). The eye was identified by the center of low-level heating near 26.3°N, 85.5°W, and surrounding the eye was an area of low-level cooling indicative of stratiform precipitation. Convective outer bands and low-level heating encircled the area of stratiform rain. The region of upper-level latent heating was shifted somewhat northwest of the storm center. At 1140 UTC on 25 August, Andrew approached the Louisiana coast and was characterized by a nearly vertical, axisymmetric structure (Fig. 16c). A large area of latent heating greater than 0.5 W m^{-3}

→

FIG. 15. Estimated surface rain rates (left column) and convective rain rates (right column) at 2259 UTC 25 Aug 1992 from the SSM/I retrieval method with the C1 constraint (top row) and C2 constraint (middle row), and from the Slidell, LA, radar (bottom row). The limit of radar coverage is indicated by a white circle superimposed on the SSM/I rain patterns. Coastlines are also indicated in white.

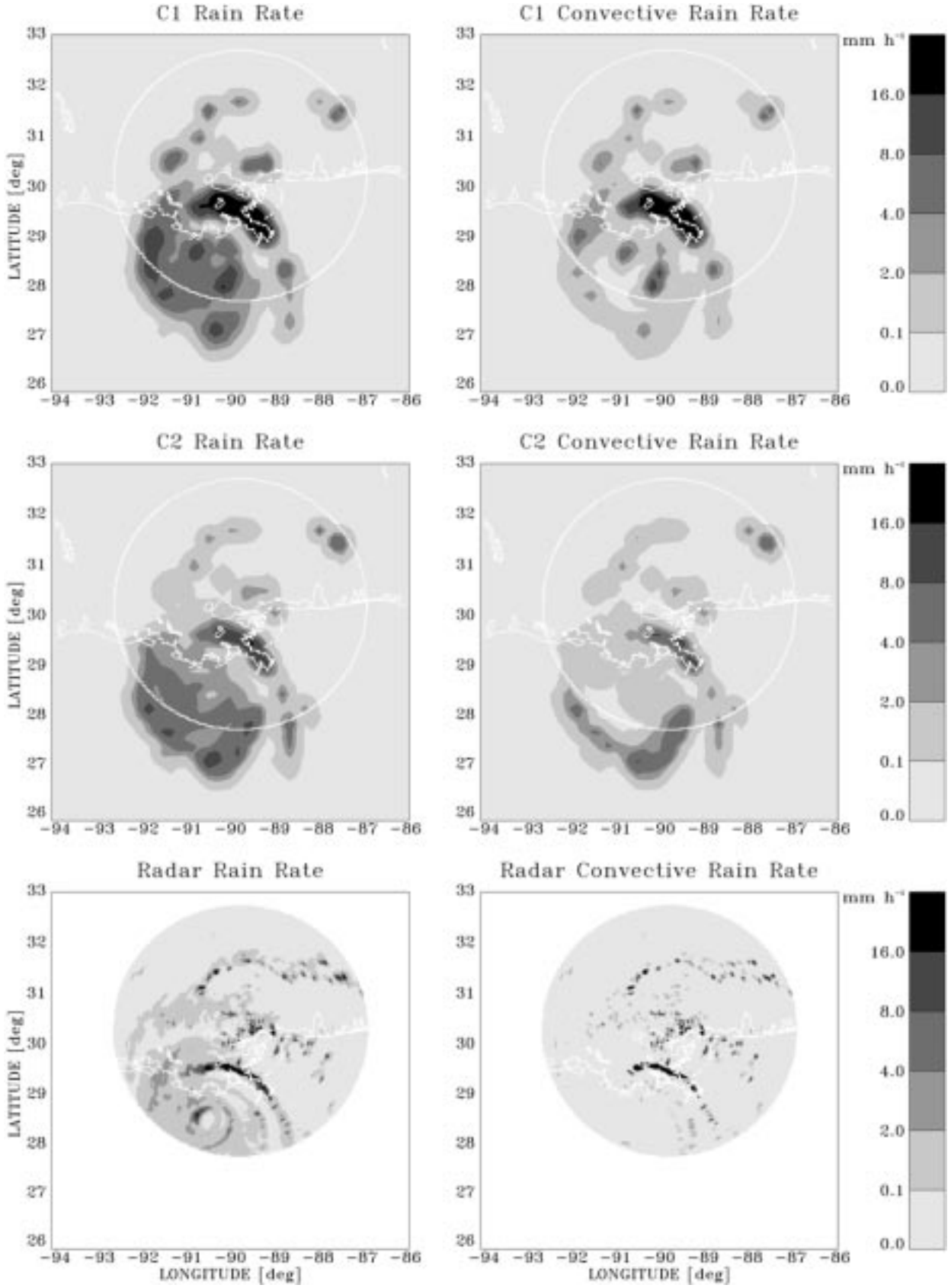
C1 Rain Rate
C1 Convective Rain Rate
C2 Rain Rate
C2 Convective Rain Rate
Radar Rain Rate
Radar Convective Rain Rate
LATITUDE [deg]
LONGITUDE [deg]
mm h⁻¹
16.0
8.0
4.0
2.0
0.1
0.0

at the 7-km level was approximately centered on the eye position near 27.2°N, 88.1°W. Just prior to landfall, Andrew assumed a more asymmetric structure characterized by spiral bands, and the patterns of low-level and upper-level heating reflected this structure (Fig. 16d). Positive latent heating at all levels was observed in the deep convective band over the Mississippi delta, with maximum heating rates exceeding 1.0 W m^{-3} at the 7-km level.

Figure 17 summarizes the progression of latent heating vertical structure in Andrew. In the figure, the retrieved latent heating profiles (area weighted) in 50-km-wide annuli centered on Andrew are plotted as a function of radius out to 300 km. Note that as Andrew intensifies from 1448 UTC on 24 August to 1140 UTC on 25 August, the upper-level latent heating maximum increases in magnitude and extends closer to the center of circulation. It has been suggested by Schubert and Hack (1982) and others that latent heating within a mature tropical cyclone's inner core, with its greater inertial stability, leads to greater warming of the core and intensification. Intensification continues through 0000 UTC on 26 August, even though heating rates have decreased substantially by 2259 UTC on 25 August. Observational studies of tropical cyclones by Steranka et al. (1986) and Rodgers and Pierce (1995) and model simulations by Rodgers et al. (1994) suggest a time lag of a few hours between increases in inner core latent heating and storm intensification.

Although low-level evaporative cooling due to stratiform rain is expected outside the eyewall region, Fig. 17 indicates predominant low-level cooling even at small radii. Deficient low-level heating is possibly linked to an underestimate of convection in the inner core: the mean retrieved convective rain flux percentage within 100-km radius is 31%, whereas aircraft observations from several storms indicate about 40% convective rain within the inner core of hurricanes (Houze et al. 1992). In this case the relatively low spatial resolution of SSM/I may contribute to errors in convective–stratiform rain separation. For example, even though Andrew had a well-defined radar eye at 2259 UTC on 25 August 1992 (Fig. 15), the eye is rather poorly resolved by the SSM/I. The mixture of eyewall precipitation signatures and nonprecipitating eye signatures in SSM/I 85.5-GHz polarization measurements can lead to ambiguity in estimates of convective areal fraction using (17) and (18). Greater spatial resolution in microwave sensors such as the TMI and AMSR should help to improve convective–stratiform rain separation in the inner cores of tropical cyclones.

6. Summary and conclusions

Calculations of the microwave radiances upwelling from model-simulated cloudy atmospheres are used to help quantify the relationships between passive microwave measurements from the SSM/I and distributions of precipitation and latent heating. It is demonstrated that these relationships are strongly dependent upon the proportion of convective and stratiform precipitation within the satellite footprint. For a given footprint-average rain rate, microwave emission and scattering are generally weaker in convective regions and stronger in stratiform regions, a result that is anticipated from previous theoretical studies of the microwave signatures from horizontally inhomogeneous (convective) and homogeneous (stratiform) precipitation fields. Signatures of latent heating are also sensitive to the proportions of convective–stratiform rain: at low levels, greater latent heating is generally associated with stronger microwave emission and scattering in convective areas, while greater evaporative cooling is associated with stronger scattering in stratiform regions. At upper levels, greater latent heating is correlated with stronger microwave emission and scattering, but for a given latent heating rate, the emission and scattering are generally greater in stratiform regions. Since the interpretation of the magnitude and even the sign of the latent heating rate can depend on the proportion of convective and stratiform rain observed by the SSM/I, the determination of this proportion is crucial for making unambiguous latent heating profile retrievals.

The impact of convective–stratiform proportion information on precipitation/latent heating profile estimates is tested within the framework of the estimated expected value or Bayesian retrieval method described by Kummerow et al. (1996) and Olson et al. (1996). An additional constraint on the areal fraction of convective rain within a specified footprint is imposed, such that only candidate profiles that are radiatively consistent with the SSM/I brightness temperatures and that have nearly the correct convective areal fraction can contribute to a solution. In applications of the retrieval method to synthetic data over water backgrounds, the correlation of estimated surface rain rates with truth at 25-km resolution increases from 0.84 to 0.92 when the additional constraint is imposed. Over 14 layers from the surface to 18-km altitude, the mean correlation of estimated latent heating rates with truth increases from 0.58 to 0.66 with the added constraint. Also, spatial smoothing of retrieved quantities and truth generally increases the correlation.

In applications of the retrieval method to actual SSM/I observations, the convective area fraction is estimated using two different empirical formulas. The first utilizes the magnitudes and gradients of ice scattering signatures at 85.5 GHz to identify areas of convective updraft (Hong et al. 1999), and the second, developed in the present study, relies on the anticorrelation of 85.5-GHz polarization difference and convective rain coverage, previously noted by Heymsfield and Fulton (1994a,b). Empirical formulas are employed to establish the relationships between SSM/I measurements and convective fraction because currently available numerical cloud model simulations do not cover the wide spectrum of

convective system types, and modeling of precipitation particle microphysics and radiative properties has not advanced to the state where polarization signatures can be reliably simulated.

Applications of the algorithm to SSM/I observations of the TOGA COARE IFA during the IOP yield rainfall rates that are better correlated with shipboard radar observations if the convective area fraction constraints are applied. Still, instantaneous precipitation fields retrieved using the two convective fraction constraints exhibit significant differences with respect to one another and with respect to radar-derived fields. It is expected that the higher spatial resolution of passive microwave radiometers such as the TMI and AMSR should help to remove ambiguities in the identification of convective–stratiform rain areas, and therefore estimated rain intensities and latent heating distributions should also improve. The reason for this is that the horizontal scale of convective regions is relatively small compared to the SSM/I 85.5-GHz footprint dimensions (13 km $\times$ 15 km). The mixture of convective and nonconvective scattering or polarization signatures in the SSM/I 85.5-GHz observations leads to ambiguity in the determination of the convective fraction. The 85.5-GHz channels of the TMI and the 89.0-GHz channels of the AMSR have footprints of 5 km $\times$ 7 km and 4 km $\times$ 6 km, respectively, [Kummerow et al. (1998) for TMI, Ashcroft and Wentz (1996) for AMSR]. Also, the addition of infrared data to the retrieval procedure may help to improve estimates of latent heating in the upper troposphere, where the microwave signal from tenuous anvils tends to be weak.

In algorithm applications to SSM/I data from TOGA COARE, the polarization-based convective fraction constraint leads to retrieved mean latent heating profiles most consistent with rawinsonde-derived Q_1 profiles, although the maximum of latent heating occurs at a lower altitude. Retrieved patterns of IOP-mean surface precipitation over the COARE LSA are similar to ECMWF-forecast rain patterns, albeit rain intensities over land areas are systematically underestimated. The ITCZ bands are characterized by a greater proportion of stratiform rain and maximum latent heating at greater altitudes than in surrounding areas.

Although intercomparisons between SSM/I latent heating distributions and similar distributions from rawinsonde budget analyses are presented in this study, with differences noted in section 5b, the validation of climate-scale, satellite-based latent heating estimates will require several such intercomparisons in climatologically dissimilar regions. For example, it is noted by Lin and Johnson (1996) that vertical heating profiles in the western Pacific consistently exhibit a maximum of heating at higher levels than those observed in the eastern Atlantic during the Global Atmospheric Research Project (GARP) Atlantic Tropical Experiment (GATE). Radar and rawinsonde networks to be established at the TRMM validation sites should provide the time series of data needed for heating profile validation. The purpose of the present work is to establish a methodology for passive microwave precipitation/latent heating profile retrieval that will be scrutinized in future studies.

SSM/I-retrieved rain rates in Hurricane Andrew are systematically higher than rain rates derived from coastal radar, although the overall patterns are correlated. The distributions of convective rainfall are dependent on the type of convective area fraction constraint imposed, especially in the hurricane eyewall. Nevertheless, the time sequence of latent heating patterns retrieved using the SSM/I algorithm (with the polarization-based convective area fraction constraint) show an increase in upper-level latent heating that becomes more concentrated near the center of circulation as Andrew intensifies. This relationship between inner core latent heating and intensification has been noted in studies by Steranka et al. (1986) and Rodgers et al. (1994).

Although differences between retrieved and rawinsonde-derived heating profiles have been identified in the current work, results from this first application of the SSM/I latent heating algorithm are encouraging. The main limitation of remote-sensing-based estimates of precipitation and latent heating from low-orbiting satellites is the intermittency of coverage in the Tropics. On average, the sampling frequency of a single low-orbiting satellite sensor is about 1 day^{-1} near the equator. Therefore, the effort to improve microwave remote sensing techniques for retrieving latent heating rates should be coupled with efforts to ''interpolate'' the relatively infrequent SSM/I, TMI, or AMSR measurements to intermediate times using frequently sampled geostationary infrared data, or by assimilating the microwave measurements into numerical weather prediction model simulations.

The possibility of using numerical models to assimilate satellite-retrieved parameters raises questions concerning the optimal retrieved parameters for assimilation. From the perspective of the microwave retrieval problem, four-dimensional model assimilation can be viewed as a means of applying dynamical constraints to a series of instantaneous satellite estimates of three-dimensional hydrometeor and latent heating fields. From this perspective, it could be argued that satellite estimates of hydrometeor distributions, rather than latent heating fields, may be optimal, since hydrometeor dis-

→

FIG. 16. Estimated vertically integrated latent heating rates (top row) and latent heating rates near 3 (middle row) and 7 km (bottom row) from the SSM/I retrieval method with the C2 constraint. Estimates from observations of Hurricane Andrew at 1448 UTC on 24 Aug 1992, and at 0156, 1140, and 2259 UTC on 25 Aug 1992, are shown in (a), (b), (c), and (d), respectively. Coastlines are indicated in white.

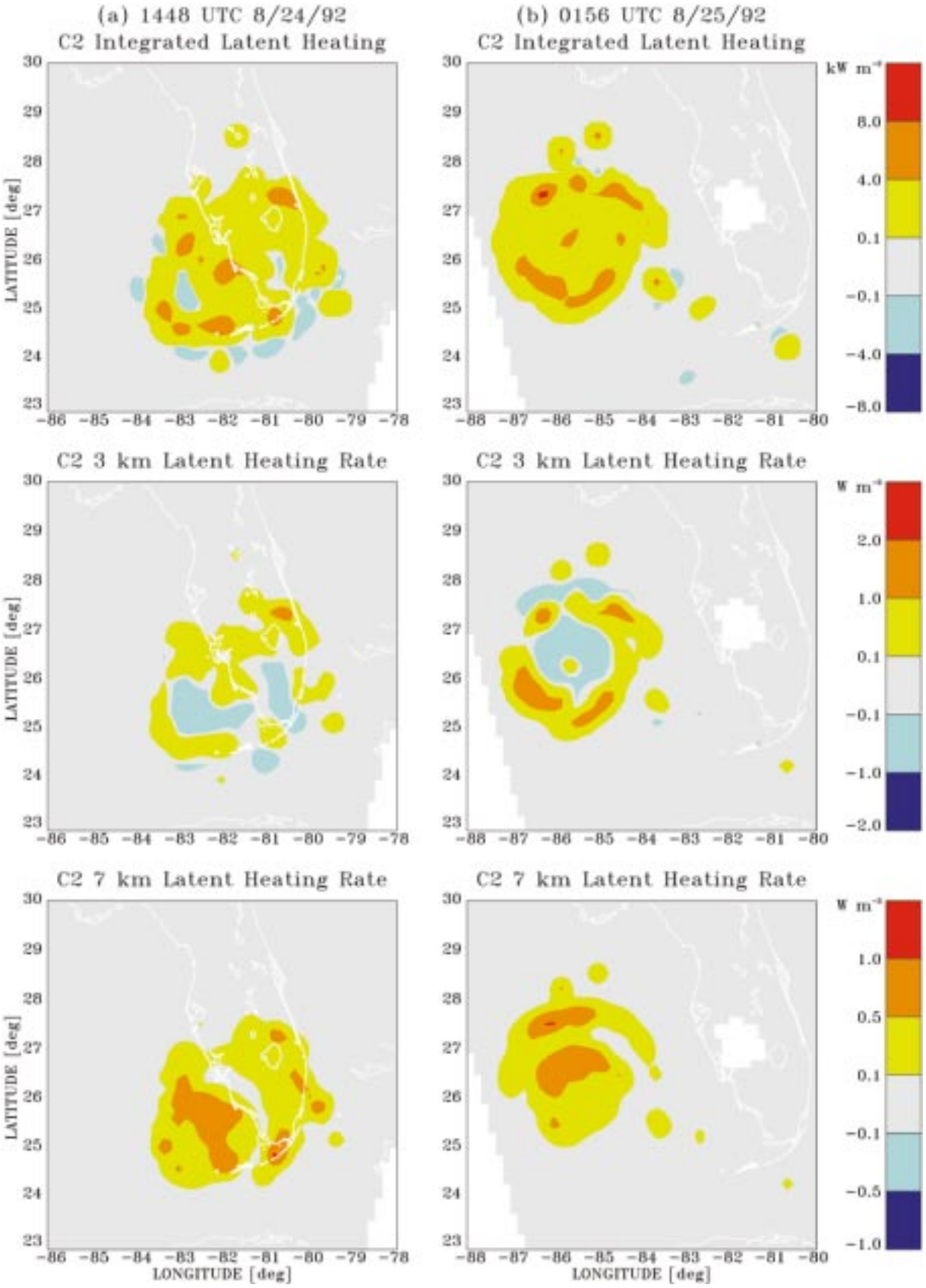
(a) 1448 UTC 8/24/92
C2 Integrated Latent Heating
(b) 0156 UTC 8/25/92
C2 Integrated Latent Heating
kW m⁻²
8.0
4.0
0.1
−0.1
−4.0
−8.0
C2 3 km Latent Heating Rate
C2 3 km Latent Heating Rate
W m⁻²
2.0
1.0
0.1
−0.1
−1.0
−2.0
C2 7 km Latent Heating Rate
C2 7 km Latent Heating Rate
W m⁻²
1.0
0.5
0.1
−0.1
−0.5
−1.0
LATITUDE [deg]
LONGITUDE [deg]

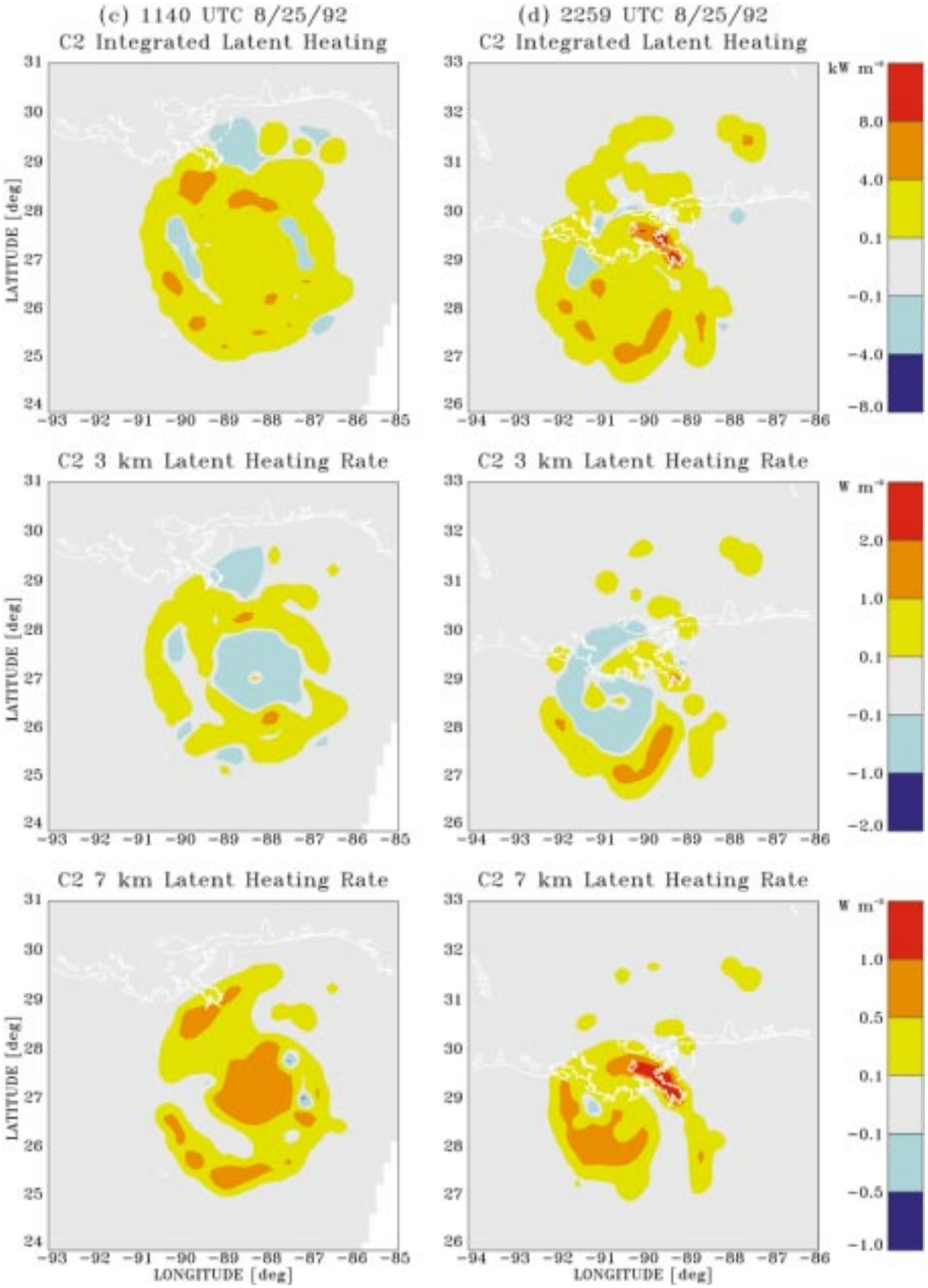

FIG. 16. (*Continued*)

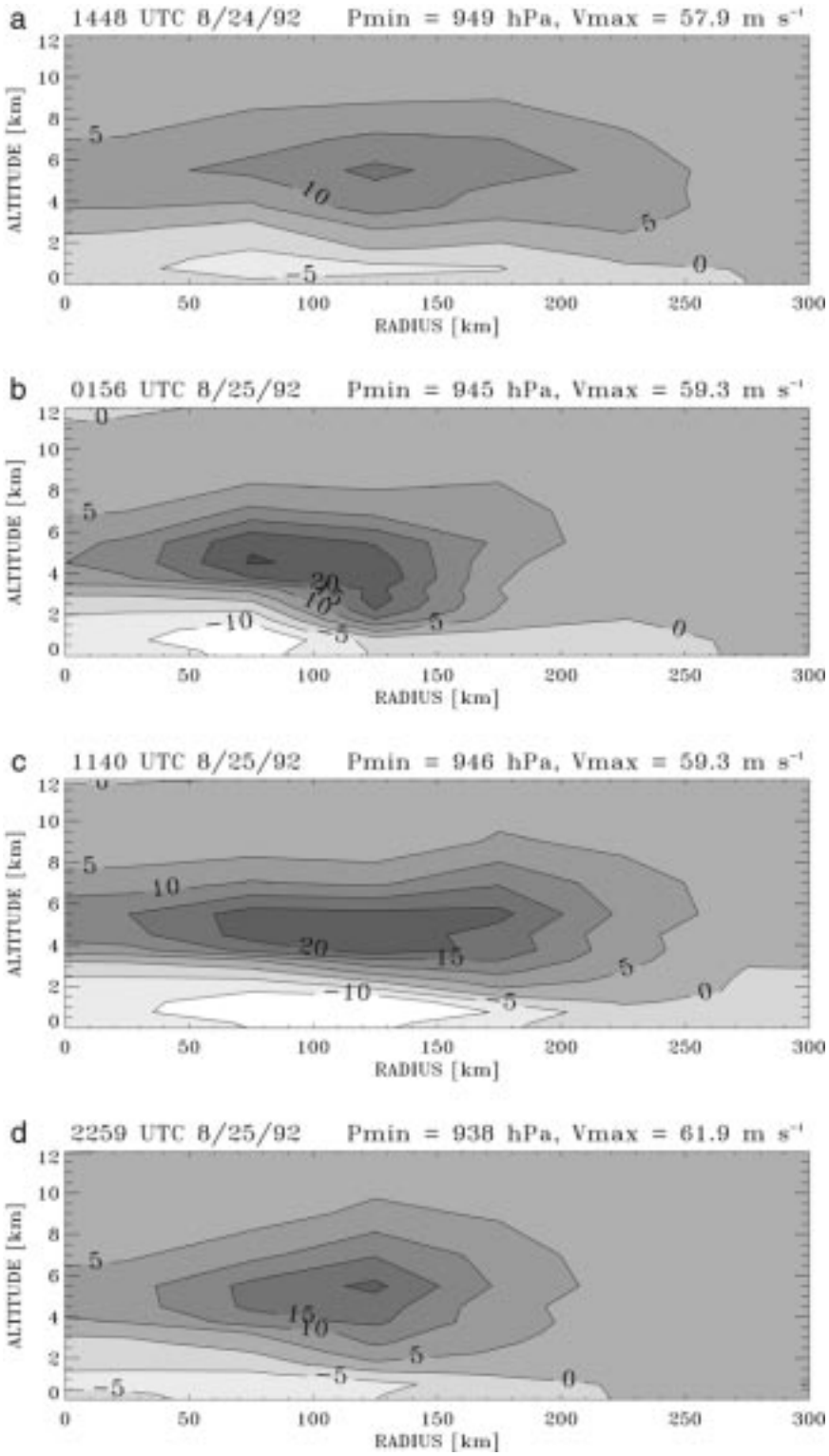

FIG. 17. Azimuthally averaged and area-weighted retrieved latent heating profiles from SSM/I, plotted as a function of radius from the center of Hurricane Andrew. Estimates in W m^{-3} from observations at 1448 UTC 24 Aug 1992, and 0156, 1140, and 2259 UTC 25 Aug 1992 are shown in (a), (b), (c), and (d), respectively.

tributions have a direct physical impact on the upwelling radiances observed by satellite microwave sensors. Latent heating fields are strongly linked to storm and cloud dynamics, and can only be inferred indirectly from microwave observations through precipitation structure. Therefore, it may be preferable to assimilate precipitating hydrometeor distributions as they become available from satellite observations, and allow the numerical weather prediction model to simulate latent heating fields that are consistent with both the evolving model dynamics and the intermittent satellite observations. Of course, this approach requires that the parameterized and/or explicit representation of cloud hydrometeor distributions in the numerical model be realistic.

Acknowledgments. The authors wish to thank Matthias Steiner, Dave Short, Grant Petty, Giulia Panegrossi, Greg Tripoli, Song Yang, Brad Ferrier, Jeff Halverson, Dan Johnson, Jeff Haferman, Nicolas Viltard, Ed Rodgers, Mohan Karyampudi, Jenni Evans, and Chung-Hsiung Sui for their assistance in this study. Xin Lin and Richard Johnson kindly provided their budget estimates of Q_1 and surface rain rates, as well as the ECMWF forecast rain rates, from TOGA COARE. We would also like to thank Peter Dodge of NOAA/AOML/HRD for providing digitized radar observations of Hurricane Andrew. This research was funded by the TRMM science program.

REFERENCES

Adler, R. F., G. J. Huffman, and P. R. Keehn, 1994: Global rain estimates from microwave-adjusted geosynchronous IR data. *Remote Sens. Rev.,* **11,** 125–152.

Anagnostou, E. N., and C. Kummerow, 1997: Stratiform and convective classification of rainfall using SSM/I 85-GHz brightness temperature measurements. *J. Atmos. Oceanic Technol.,* **14,** 570–575.

Anthes, R. A., 1982: *Tropical Cyclones—Their Evolution, Structure and Effects. Meteor. Monogr.,* No. 41, Amer. Meteor. Soc., 208 pp.

Ashcroft, P., and F. J. Wentz, 1996: Algorithm theoretical basis document—AMSR level-1C algorithm. RSS Tech. Rep. 121296, Remote Sensing Systems, Santa Rosa, CA, 26 pp. [Available from Remote Sensing Systems, 1101 College Ave., Santa Rosa, CA 95404.]

Biggerstaff, M. I., and R. A. Houze Jr., 1993: Kinematics and microphysics of the 10–11 June 1985 squall line. *J. Atmos. Sci.,* **50,** 3091–3110.

Black, M. L., and H. E. Willoughby, 1992: The concentric eyewall cycle of Hurricane Gilbert. *Mon. Wea. Rev.,* **120,** 947–957.

Braun, S. A., and R. A. Houze Jr., 1996: The heat budget of a midlatitude squall line and implications for potential vorticity production. *J. Atmos. Sci.,* **53,** 1217–1240.

Chang, C.-P., and H. Lim, 1988: Kelvin wave-CISK: A possible mechanism for the 30–50 day oscillations. *J. Atmos. Sci.,* **45,** 1709–1720.

Churchill, D. D., and R. A. Houze Jr., 1984: Development and structure of winter monsoon cloud clusters on 10 December 1978. *J. Atmos. Sci.,* **41,** 933–960.

DeMaria, M., 1985: Linear response of a stratified tropical atmosphere to convective forcing. *J. Atmos. Sci.,* **42,** 1944–1959.

Eliassen, A., 1952: Slow thermally or frictionally controlled meridional circulation in a circular vortex. *Astrophys. Norv.,* **5,** 19–60.

Ferrier, B. S., J. Simpson, and W.-K. Tao, 1996: Factors responsible for precipitation efficiencies in midlatitude and tropical squall line simulations. *Mon. Wea. Rev.,* **124,** 2100–2125.

Flatau, P., G. J. Tripoli, J. Berlinder, and W. Cotton, 1989: The CSU-RAMS cloud microphysics model: General theory and code documentation. Atmospheric Sciences Rep. 451, Colorado State University, Fort Collins, CO, 88 pp. [Available from Dept. of Atmospheric Science, Colorado State University, Fort Collins, CO 80523.]

Frank, W. M., H. Wang, and J. L. McBride, 1996: Rawinsonde budget analyses during the TOGA COARE IOP. *J. Atmos. Sci.,* **53,** 1761–1780.

Hartmann, D. L., H. H. Hendon, and R. A. Houze Jr., 1984: Some implications of the mesoscale circulations in tropical cloud clusters of large-scale dynamics and climate. *J. Atmos. Sci.,* **41,** 113–121.

Hauser, D., F. Roux, and P. Amayenc, 1988: Comparison of two methods for the retrieval of thermodynamic and microphysical variables from Doppler-radar measurements: Application to the case of a tropical squall line. *J. Atmos. Sci.,* **45,** 1285–1303.

Heymsfield, G. M., and R. Fulton, 1994a: Passive microwave and infrared structure of mesoscale convective systems. *Meteor. Atmos. Phys.,* **54,** 123–139.

——, and ——, 1994b: Passive microwave structure of severe tornadic storms on 16 November 1987. *Mon. Wea. Rev.,* **122,** 2587–2595.

Hollinger, J., R. Lo, G. Poe, R. Savage, and J. Peirce, 1987: Special Sensor Microwave/Imager user's guide. Naval Research Laboratory, Washington, DC, 120 pp. [Available from Naval Research Laboratory, Washington, DC 20375.]

Hong, Y., C. D. Kummerow, and W. S. Olson, 1999: Separation of convective and stratiform precipitation using microwave brightness temperature. *J. Appl. Meteor.,* in press.

Houze, R. A., Jr., 1989: Observed structure of mesoscale convective systems and implications for large-scale heating. *Quart. J. Roy. Meteor. Soc.,* **115,** 425–461.

——, F. D. Marks Jr., and R. A. Black, 1992: Dual-aircraft investigation of the inner core of Hurricane Norbert. Part II: Mesoscale distribution of ice particles. *J. Atmos. Sci.,* **49,** 943–962.

Huffman, G. J., R. F. Adler, B. Rudolf, U. Schneider, and P. R. Keehn, 1995: Global precipitation estimates based on a technique for combining satellite-based estimates, rain gauge analysis, and NWP model precipitation information. *J. Climate,* **8,** 1284–1295.

Johnson, R. H., 1976: The role of convective-scale precipitation downdrafts in cumulus and synoptic–scale interactions. *J. Atmos. Sci.,* **33,** 1890–1910.

Jorgensen, D. P., T. J. Matejka, D. Johnson, and M. A. LeMone, 1994: A TOGA/COARE squall line seen by multiple Doppler radars. Preprints, *Sixth Conf. on Mesoscale Processes,* Portland, OR, Amer. Meteor. Soc., 25–28.

Karstens, U., C. Simmer, and E. Ruprecht, 1994: Remote sensing of cloud liquid water. *Meteor. Atmos. Phys.,* **54,** 157–171.

Karyampudi, V. M., G. S. Lai, and J. Manobianco, 1998: Impact of initial conditions, rainfall assimiliation, and cumulus parameterization on simulations of Hurricane Florence (1988). *Mon. Wea. Rev.,* **126,** 3077–3101.

Kasahara, A., A. P. Mizzi, and L. J. Donner, 1992: Impact of cumulus initialization on the spinup of precipitation forecasts in the tropics. *Mon. Wea. Rev.,* **120,** 1360–1380.

Krishnamurti, T. N., J. Xue, H. S. Bedi, K. Ingles, and O. Oosterhof, 1991: Physical initialization for numerical weather prediction over the tropics. *Tellus,* **43AB,** 53–81.

Kummerow, C., 1998: Beamfilling errors in passive microwave rainfall retrievals. *J. Appl. Meteor.,* **37,** 356–370.

——, W. S. Olson, and L. Giglio, 1996: A simplified scheme for obtaining precipitation and vertical hydrometeor profiles from passive microwave sensors. *IEEE Trans. Geosci. Remote Sens.,* **34,** 1213–1232.

——, W. Barnes, T. Kozu, J. Shiue, and J. Simpson, 1998: The Tropical Rainfall Measuring Mission (TRMM) sensor package. *J. Atmos. Oceanic Technol.,* **15,** 809–817.

Lau, K.-M., and L. Peng, 1987: Origin of the low-frequency (intraseasonal) oscillation in the tropical atmosphere. *J. Atmos. Sci.,* **44,** 950–972.

Lin, X., and R. H. Johnson, 1996: Heating, moistening, and rainfall over the western Pacific warm pool during TOGA COARE. *J. Atmos. Sci.,* **53,** 3367–3383.

Mapes, B. E., and R. A. Houze Jr., 1995: Diabatic divergence profiles in western Pacific mesoscale convective systems. *J. Atmos. Sci.,* **52,** 1807–1828.

Marks, F., 1985: Evolution of the structure of precipitation in Hurricane Allen (1980). *Mon. Wea. Rev.,* **113,** 909–930.

Mayfield, M., L. Avila, and E. N. Rappaport, 1994: Atlantic hurricane season of 1992. *Mon. Wea. Rev.,* **122,** 517–538.

Ogura, Y., and H.-R. Cho, 1973: Diagnositic determination of cumulus cloud populations from observed large-scale variables. *J. Atmos. Sci.,* **30,** 1276–1286.

Olson, W. S., C. D. Kummerow, G. M. Heymsfield, and L. Giglio, 1996: A method for combined passive–active microwave retrievals of cloud and precipitation profiles. *J. Appl. Meteor.,* **35,** 1763–1789.

Panegrossi, G., and Coauthors, 1998: Use of cloud model microphysics for passive microwave-based precipitation retrieval: Significance of consistency between model and measurement manifolds. *J. Atmos. Sci.,* **55,** 1644–1673.

Peng, M. S., and S. W. Chang, 1996: Impacts of SSM/I retrieved rainfall rates on numerical prediction of a tropical cyclone. *Mon. Wea. Rev.,* **124,** 1181–1198.

Petty, G. W., 1994: Physical retrieval of over-ocean rain rate from multichannel microwave imagery. Part I: Theoretical characteristics of normalized polarization and scattering indices. *Meteor. Atmos. Phys.,* **54,** 79–100.

——, and J. Turk, 1996: Observed multichannel microwave signatures of spatially extensive precipitation in tropical cyclones. Preprints, *Eighth Conf. on Satellite Meteorology and Oceanography,* Atlanta, GA, Amer. Meteor. Soc., 291–294.

Raymond, W. H., W. S. Olson, and G. Callan, 1995: Diabatic forcing and initialization with assimilation of cloud water and rainwater in a forecast model. *Mon. Wea. Rev.,* **123,** 366–382.

Rickenbach, T. M., and S. A. Rutledge, 1998: Convection in TOGA COARE: Horizontal scale, morphology, and rainfall production. *J. Atmos. Sci.,* **55,** 2715–2729.

Rodgers, E. B., and R. F. Adler, 1981: Tropical cyclone rainfall characteristics as determined from a satellite passive microwave radiometer. *Mon. Wea. Rev.,* **109,** 506–521.

——, and H. F. Pierce, 1995: A satellite observational study of precipitation characteristics in western North Pacific tropical cyclones. *J. Appl. Meteor.,* **34,** 2587–2599.

——, S. W. Chang, and H. F. Pierce, 1994: A satellite observational and numerical study of the precipitation characteristics in western North Atlantic tropical cyclones. *J. Appl. Meteor.,* **33,** 129–139.

Rutledge, S. A., and P. V. Hobbs, 1983: The mesoscale and microscale structure and organization of clouds and precipitation in midlatitude cyclones. Part VIII: A model for the ''seeder-feeder'' process in warm-frontal rainbands. *J. Atmos. Sci.,* **40,** 1185–1206.

Schols, J., J. Hafermann, J. Weinman, C. Prabhakara, M. Cadeddu, and C. Kummerow, 1997: Polarized microwave radiation model of melting deformed hydrometeors. Preprints, *Ninth Conf. on Atmospheric Radiation,* Long Beach, CA, Amer. Meteor. Soc., 270–273.

Schubert, W. H., and J. J. Hack, 1982: Inertial stability and tropical cyclone development. *J. Atmos. Sci.,* **39,** 1687–1697.

Shapiro, L. J., and H. E. Willoughby, 1982: The response of balanced hurricanes to local sources of heat and momentum. *J. Atmos. Sci.,* **39,** 378–394.

Short, D. A., P. A. Kucera, B. S. Ferrier, J. C. Gerlach, S. A. Rutledge, and O. Thiele, 1997: Shipboard radar rainfall patterns within the TOGA COARE IFA. *Bull. Amer. Meteor. Soc.,* **78,** 2817–2836.

Simpson, J., R. F. Adler, and G. R. North, 1988: A proposed Tropical Rainfall Measuring Mission (TRMM) satellite. *Bull. Amer. Meteor. Soc.,* **69,** 278–295.

Smith, E. A., X. Xiang, A. Mugnai, and G. J. Tripoli, 1994: Design of an inversion-based precipitation profile retrieval algorithm using an explicit cloud model for initial guess microphysics. *Meteor. Atmos. Phys.,* **54,** 53–78.

Spencer, R. W., H. M. Goodman, and R. E. Hood, 1989: Precipitation retrieval over land and ocean with SSM/I: Identification and characteristics of the scattering signal. *J. Atmos. Oceanic Technol.,* **6,** 254–273.

Steranka, J., E. B. Rodgers, and R. C. Gentry, 1986: The relationship between satellite measured convective bursts and tropical cyclone intensification. *Mon. Wea. Rev.,* **114,** 1539–1546.

Sui, C.-H., and K.-M. Lau, 1989: Origin of the low-frequency (intraseasonal) oscillations in the tropical atmosphere. Part II: Structure and propagation of mobile wave-CISK modes and their modification by lower boundary forcings. *J. Atmos. Sci.,* **46,** 37–56.

Tao, W.-K., and J. Simpson, 1993: Goddard Cumulus Ensemble Model. Part I: Model description. *Terrest. Atmos. Oceanic Sci.,* **4,** 35–72.

——, ——, S. Lang, M. McCumber, R. Adler, and R. Penc, 1990: An algorithm to estimate the heating budget from vertical hydrometeor profiles. *J. Appl. Meteor.,* **29,** 1232–1244.

——, ——, C.-H. Sui, B. Ferrier, S. Lang, J. Scala, M.-D. Chou, and K. Pickering, 1993a: Heating, moisture, and water budgets of tropical and midlatitude squall lines: Comparisons and sensitivity to longwave radiation. *J. Atmos. Sci.,* **50,** 673–690.

——, S. Lang, J. Simpson, and R. Adler, 1993b: Retrieval algorithms for estimating the vertical profiles of latent heat release: Their applications for TRMM. *J. Meteor. Soc. Japan,* **71,** 685–700.

Tripoli, G. J., 1992a: A nonhydrostatic model designed to simulate scale interaction. *Mon. Wea. Rev.,* **120,** 1342–1359.

——, 1992b: An explicit three-dimensional nonhydrostatic numerical simulation of a tropical cyclone. *Meteor. Atmos. Phys.,* **49,** 229–254.

Webster, P. J., and R. Lucas, 1992: The TOGA Coupled Ocean–Atmosphere Response Experiment. *Bull. Amer. Meteor. Soc.,* **73,** 1377–1416.

Willoughby, H. E., 1990: Temporal changes of the primary circulation in tropical cyclones. *J. Atmos. Sci.,* **47,** 242–264.

——, J. A. Clos, and M. G. Shoreibah, 1982: Concentric eye walls, secondary wind maxima, and the evolution of the hurricane vortex. *J. Atmos. Sci.,* **39,** 395–411.

Woodley, W. L., 1970: Precipitation results from a pyrotechnic cumulus seeding experiment. *J. Appl. Meteor.,* **9,** 242–257.

Yanai, M., S. Esbensen, and J. H. Chu, 1973: Determination of bulk properties of tropical cloud clusters from large-scale heat and moisture budgets. *J. Atmos. Sci.,* **30,** 611–627.

Yang, S., and E. A. Smith, 1999: Moisture budget analysis of TOGA COARE area using SSM/I–retrieved latent heating and large scale Q_2 estimates. *J. Atmos. Oceanic Technol.,* **16,** 633–655.